JGR Solid Earth

Key Points:

- More preexisting damage and larger steps produce more off-fault deformation
- The fault parallel velocity produces larger and more temporally continuous regions of high velocities than the other components
- The shear and volumetric strains produce similarly sized regions preceding failure

Correspondence to:

J. A. McBeck,
j.a.mcbeck@geo.uio.no

Precursory Off-Fault Deformation in Restraining and Releasing Step Overs: Insights From Discrete Element Method Models

J. A. McBeck[1] , Y. Ben-Zion[2] , X. Zhou[2], and F. Renard[1,3]

[1]The Njord Centre, Departments of Geosciences and Physics, University of Oslo, Oslo, Norway, [2]Department of Earth Sciences, Southern California Earthquake Center, University of Southern California, Los Angeles, CA, USA, [3]ISTerre, University Grenoble Alpes, Grenoble INP, University Savoie Mont Blanc, CNRS, IRD, University Gustave Eiffel, Grenoble, France

Abstract Accelerating geophysical activity is detected preceding some, but not all, large earthquakes. This observation may indicate that no precursors occur before some earthquakes, or that the instrumentation lacks the required sensitivity. To aid crustal monitoring efforts, we use discrete element method models to identify the locations and styles of deformation that may provide useful information about approaching fault reactivation. We model the reactivation of two healed rough faults in a variety of step over configurations, embedded in a host rock with varying amounts of damage subject to shear velocity loading parallel to the faults. Both the fault geometry and ratio of fault to host rock strength control the amount of off-fault deformation. Consistent with field observations, models with larger steps and more preexisting host rock damage produce higher amounts of off-fault deformation. We assess the size of the continuous regions of high velocities and strains to compare the value of the precursory information of each velocity and strain component. Comparing the three components of the velocity vector suggests that the fault-parallel velocity produces the largest and most temporally continuous regions of elevated velocity. The size of these regions increases toward failure, indicating the usefulness of tracking this component. Comparing the volumetric and shear components of the three-dimensional strain tensor suggests that during most of the interseismic period, the shear strain provides more information about approaching fault slip than the volumetric strain. However, in the days and months preceding fault reactivation, both the shear and volumetric strains provide similarly valuable information.

Plain Language Summary Variations in geophysical properties preceding some large earthquakes suggest the possibility of using such signals to forecast the timing of large events. However, detectable precursors do not appear to precede some earthquakes. To improve crustal monitoring efforts, we use numerical models to simulate deformation preceding the reactivation of two faults in a variety of geometries. Contrary to expectations, similarly strong precursory deformation occurs outside of the zones of healed faults as within these zones. In agreement with previous work, decreasing the strength of the crust and increasing the geometric complexity of the fault network promotes off-fault deformation. By examining the three-dimensional velocity and strain components preceding fault reactivation, we find that the fault parallel velocity component, the shear strain, and the volumetric strain may produce the most systematic, and thus perhaps the most detectable, precursory information in the months and days preceding fault reactivation.

1. Introduction

Observations suggest that geophysical activity in the volume of crust surrounding major faults may change in the years, days and hours before some large earthquakes (e.g., Cicerone et al., 2009; Kato & Ben-Zion, 2021). Laboratory experiments indicate that a phase of accelerating slow slip precedes seismic slip, suggesting that physical processes evolve in the time leading to catastrophic failure (e.g., Dieterich, 1978; Ohnaka, 1996). However, some large earthquakes do not appear to produce detectable signals (e.g., Bakun et al., 2005; Borcherdt et al., 2006), casting doubt on the feasibility of forecasting the timing of large earthquakes. This lack of detection may arise in part from inadequate sensitivity or precision of the recording instruments or post-processing methods, rather than the absence of precursors. For example, detailed analysis of seismic waveforms recorded by dense arrays around the rupture zone of the 2019 Ridgecrest earthquake reveals previously undetected foreshocks (Meng & Fan, 2021). Thus, increasing the data quality produced more evidence of precursory activity. More generally,

crustal deformation associated with large earthquakes is multiscale and diverse, and involves both fracturing and frictional processes along and surrounding structures with wide ranges of geometrical and material heterogeneities (e.g., Ben-Zion, 2008). These factors complicate the ability of detecting systematic precursors to large earthquakes. Two key efforts may improve crustal monitoring, and the corresponding ability to detect precursors: (a) identifying the locations relative to the main faults that produce the strongest precursory activity, and (b) constraining the direction of ground motion or component of the strain tensor that may produce the strongest precursory signals. Here, we use three-dimensional discrete element method (DEM) simulations of growing fault networks to examine the evolving positions and styles of precursors.

2. Background

2.1. The Partitioning of On-Fault and Off-Fault Deformation

Examining how fault networks partition deformation on- and off-fault may provide insight into the location of potential precursors to fault slip. Faults are associated with zones of weakness relative to the host rock that can localize deformation, including preseismic damage and foreshocks (e.g., Ben-Zion & Zaliapin, 2020). Consequently, one may expect that the strongest precursory deformation would occur near or within the principal slip zone. However, the volume of the crust surrounding the main faults, including both the damage zone and surrounding host rock, can host significant levels of seismic activity (e.g., Cheng et al., 2018; Wollin et al., 2018). Damage zones are characterized by lower seismic velocities, lower rigidity, and intense microfracturing compared to the host rock, and have thicknesses of 1–5 km perpendicular to the main fault plane (e.g., Allam & Ben-Zion, 2012; Ben-Zion et al., 2003; Cochran et al., 2009; Faulkner et al., 2006; Spudich & Olsen, 2001; Zigone et al., 2015). The ubiquity of such damage zones around large faults highlights the prevalence of deformation that occurs outside of the principal slip zone, that is, off-fault deformation.

Geophysical and field observations suggest that the amount of off-fault deformation can vary significantly, from zero to up to tens of percent of the total deformation (e.g., Herbert et al., 2014; Kimurah et al., 2004; Milliner et al., 2015, 2016; Nelson & Jones, 1987; Rockwell et al., 2002; Shelef & Oskin, 2010). The structural complexity of a fault system influences the partitioning of on- and off-fault deformation (e.g., DeLong et al., 2010; Lindsey et al., 2014; Milliner et al., 2015, 2016; Oskin et al., 2007; Scott et al., 2018; Teran et al., 2015; Wechsler et al., 2009). For example, an analysis of six large earthquakes found that structurally complex faults hosted less of the total slip of these earthquakes (50%–60%) than geometrically simpler faults (85%–95%) (Dolan & Haravitch, 2014). Thus, the crustal locations that host the most pronounced deformation preceding fault slip may not occur within the preexisting fault zone. Moreover, the likelihood of identifying such precursors within the fault zone may vary depending on the maturity of the fault zones. Simpler, more mature fault zones may tend to produce the strongest precursors within the fault zone, whereas more complex fault zones may tend to produce strong precursors both within and outside the fault zone.

2.2. Styles of Precursory Deformation

In addition to identifying the locations that most likely produce the strongest precursors, it may also be useful to determine which components of the displacement and strain tensor produce the most valuable information about the timing of failure. If the uplift or subsidence of the surface provides more systematic information about imminent fault slip than the horizontal components of ground motion, monitoring efforts should focus on measuring the vertical components. Similarly, if the volumetric strain provides more systematic precursory information than the shear strain, monitoring efforts may benefit from closely tracking the volumetric component of deformation. Observations of precursory geophysical activity suggest that dilation of the crust produces some of these signals, including perturbations in seismic wave properties documented in laboratory experiments (e.g., Chen et al., 1993; Hedayat et al., 2014; Shreedharan et al., 2020) and in the crust (e.g., Malagnini et al., 2019; Niu et al., 2008; Whitcomb et al., 1973). However, dilation alone cannot explain the spectrum of precursory activity. For example, the ratio of the compressional to shear wave velocity decreases before some earthquakes, but then increases again shortly before the event (e.g., Dieterich, 1978). Dilation of the crust via fracture propagation and opening may produce the initial decrease in the velocity ratio, but an additional mechanism is required for the subsequent increase. One explanation for the recovery of the velocity ratio is the diffusion-dilatancy hypothesis: first dilation

reduces the velocity ratio, and then when the rate of water flow exceeds the dilative strain rate, the ratio begins to recover (Nur, 1972). An alternative explanation may involve the transition from early aseismic slip to coseismic slip (Dieterich, 1978).

2.3. Step Over Development

Fault networks develop through the coalescence and linkage of individual fault segments. Early in fault development, isolated fault segments may propagate and/or open, and with increasing displacement, the neighboring segments tend to link (Riedel, 1929). The distance between these segments depends on the thickness of the brittle portion of the crust (e.g., Jiao et al., 2021). Depending on the loading conditions and preexisting geometry of fault segments, the volume of crust between the tips of neighboring faults may develop contraction or extension (e.g., Cooke et al., 2013; Cunningham & Mann, 2007; Dooley & Schreurs, 2012; Lunn et al., 2008). Fault segments that produce contraction and extension are referred to as restraining and releasing steps, respectively (Mann, 2007). The initial spacing between fault segments in both the fault-parallel and fault-perpendicular directions influences the geometry of the releasing or restraining step that subsequently develops (Mann, 2007). Greater overlap in the fault-parallel direction promotes rhomboidal fault geometries, whereas greater underlap promotes spindle-shaped fault intersections. Larger separation distances between the faults, in the fault-perpendicular direction, also promotes rhomboidal fault geometries.

The systematic influence of the initial fault geometry on (a) the resulting fault network, (b) the stress field between the faults, and (c) the spatial distribution of the damage between the fault segments in step overs provides a unique opportunity to use these systems to represent endmembers of fault interaction. By varying the fault-perpendicular separation distance, we may observe how the style and location of precursory deformation vary in systems dominated by extension and contraction, that is, in releasing and restraining step overs, respectively. In addition, because fault networks evolve from isolated smaller segments to connected, larger, through-going faults (e.g., Ben-Zion & Sammis, 2003; Manighetti et al., 2007; Otsuki & Dilov, 2005), testing the influence of increasing the separation distance enables systematic comparison of the influence of structural maturity on the style and location of precursors. Comparison of km-scale seismogenic fault networks indicates that the ratio of the maximum width of a step over to the segment length within crustal fault networks decreases with increasing maturity (Manighetti et al., 2021). Consequently, fault networks with smaller separation distance represent more structurally mature fault systems with greater localization than more immature systems that tend to have larger offsets between the fault segments. Moreover, despite the ubiquity of step overs and bends in the crust, many of the laboratory analyses that have recognized precursors to fault slip and failure identified these signals in systems with intact rock or sliding blocks with one preexisting, cohesionless fault surface (McBeck, Aiken et al., 2020; Shreedharan et al., 2020).

In the present study, we use three-dimensional discrete element method (DEM) simulations of growing fault networks with two underlapping faults in step over configurations to examine the evolving positions and styles of precursors. We systematically vary the fault-perpendicular distance between preexisting faults in the step overs, from releasing to restraining step overs, because fault zone complexity controls the magnitude of off-fault deformation (e.g., Dolan & Haravitch, 2014), and thus perhaps the position of precursors relative to the main fault. This suite of models is not meant to simulate a particular crustal fault zone, but instead to represent various cases of potential fault development: from releasing to restraining steps, and coplanar faults.

The other key characteristic of a fault network that may influence the location and nature of precursory deformation is the relative strength of the host rock to the fault. More off-fault deformation may occur around faults embedded in weaker material than stronger host rock (e.g., Milliner et al., 2015; Rockwell et al., 2002; Titus et al., 2011; Zinke et al., 2014). Consequently, we vary the amount of preexisting host rock damage, and thereby the relative strength of the host rock and main fault. Although damage can develop preferentially on one side of a fault (Berg & Skar, 2005; Dor et al., 2006), here we model more generic systems in which diffuse damage is distributed throughout the model in order to simulate fault development in a statistically uniform host rock. For this suite of models, we examine the evolving deformation field preceding motion along preexisting faults that have non-zero cohesion and stiffness, for example, healed faults. We compare the locations and styles of precursory deformation in the three-dimensional displacement and strain fields generated in the model simulations.
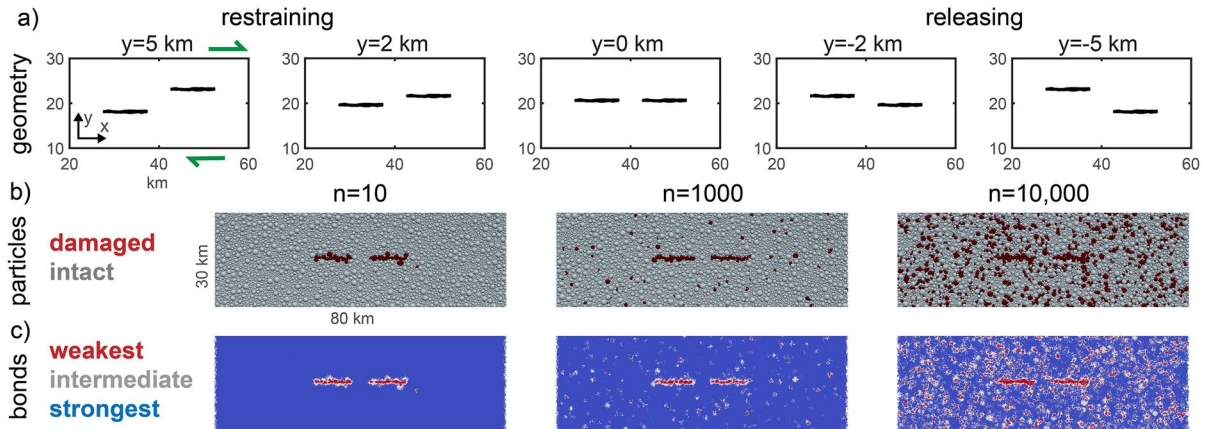
Figure 1. Fault configurations and amounts of damage. (a) Geometries of restraining and releasing step overs, and (b) particles and (c) bonds in coplanar ($y = 0$ km) simulations with varying amounts of damage. Geometries show an inset of the $80 \times 40 \times 10$ km models. (b) Particles are colored by the type of material they simulate. The red particles represent the more damaged rock within the preexisting fault zone, and diffuse damage spread throughout the model. The gray particles represent the relatively more intact host rock. (c) To produce these different types of materials, we prescribe different cohesions and stiffnesses to three sets of bonds. The red bonds simulate the weakest material (on-fault and preexisting damage) and the blue bonds represent the strongest material (off-fault). The red bonds connect the damaged particles, and the blue bonds connect the intact particles. The gray bonds connect damaged and intact particle pairs.

3. Methods

3.1. ESyS-Particle

We use the ESyS-Particle numerical framework to build the DEM models (Abe et al., 2004). ESyS-Particle uses indestructible spherical particles to simulate the deformation of rocks and other materials. Bonds may connect the particles. Both the particles and bonds have prescribed microparameters, such as friction coefficients, cohesion, and stiffness. The microparameters, and the packing of the particles and bonds, control the macroscopic mechanical behavior of the model. ESyS-Particle benefits from particle packing algorithms that produce relatively low porosity (10%–20%) models with particle radii of 0.1–1 model units. ESyS-Particle does not have an inherent length scale (Abe et al., 2004, 2011; Place et al., 2002), and so the user decides the length scale that one model unit represents.

Bonds can break during deformation if the forces acting on them exceed a Coulomb criterion. The Coulomb criterion is derived from the prescribed microparameters (cohesion and friction) of the bonds. Unbonded particles experience frictional and elastic forces. Several processes contribute to off-fault damage production in crustal fault systems, including damage produced during earthquake propagation (e.g., Andrews, 2005; Rice et al., 2005; Xu et al., 2015). Because our DEM models are quasi-static, we cannot include the influence of dynamic rupture. Instead, we focus on the quasi-static brittle deformation that occurs due to long term fault propagation, slip, opening, and linkage.

3.2. Model Construction

To assess the influence of fault geometry and preexisting host rock damage on the nature of precursors, we build simulations of step overs with varying geometries and host rock properties. The dimensions of the model are 80 km (along the x-axis), 40 km (y-axis), and 10 km thick (z-axis). The models contain two parallel faults 10 km long that are separated by half a fault length (5 km) in the x-direction (Figure 1a). We vary the vertical spacing, y, between the faults to simulate two restraining step over configurations ($y > 0$), two releasing step over configurations ($y < 0$), and a coplanar system ($y = 0$). The faults extend from the front to the back of the model in the z-direction. These models are similar to those used in previous work (McBeck et al., 2021), except here we include two faults instead of one.

The faults have roughness parameters, including a set of Hurst exponents parallel and perpendicular to the fault strike, that match natural faults (McBeck et al., 2021). We create these faults by building mesh surfaces with the prescribed roughness parameters at the dimensions of the model and the desired location. We then label the
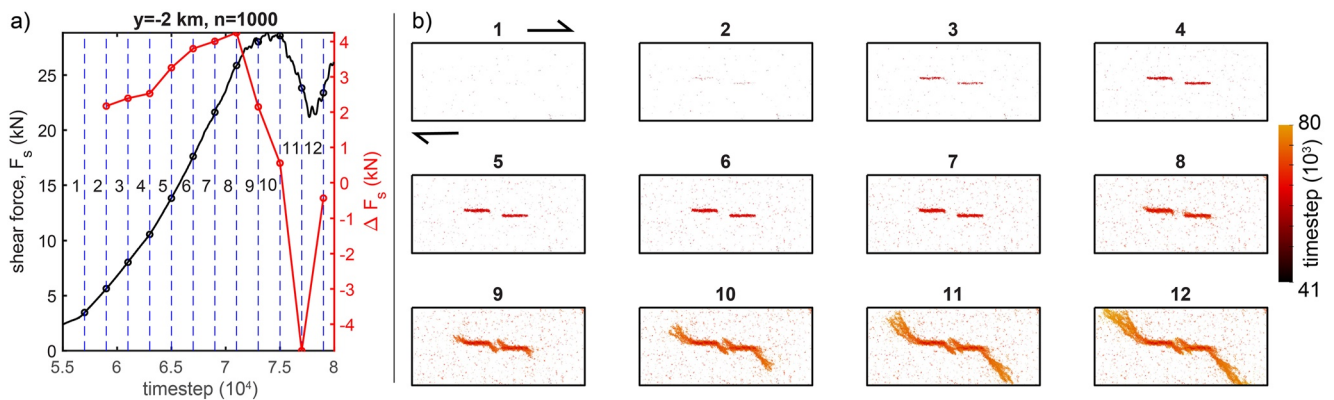
Figure 2. Characteristic fault network development for the model with intermediate damage, $n = 1,000$, and a releasing step over configuration with $y = -2$ km. (a) Macroscopic shear force acting on the top and bottom walls of the model, F_s (black), and the change in F_s between the snapshots of the model shown in (b) (red). (b) Fracture network of the models at the times indicated on (a) with blue dashed lines. The colors of the fractures indicate the timestep when the fracture developed (i.e., when the bond between two particles broke).

particles within 1 km of this surface as damaged, and the remaining particles as intact. We also vary the amount of diffuse preexisting damage included in the model with a similar method. We place varying numbers of seed particles throughout the model, $n = 10$–10,000, and then label particles near these seeds as damaged, the radius of the largest particle. Higher n produces systems with more damaged crust.

Thus, the models contain two types of particles. These two types correspond to the damaged material, including the preexisting fault damage zone and diffuse off-fault damage, and the more intact host rock in the simulations. In Figure 1b, the red particles show the more damaged rock within the preexisting fault zone, and diffuse damage spread throughout the model. The gray particles show the more intact host rock. To produce these different types of materials, we prescribe different cohesions and stiffnesses to three sets of bonds (Figure 1c). The three sets of bonds represent the (a) intact rock (blue bonds in Figure 1c), (b) damaged material (red bonds in Figure 1c), and (c) material with strength and stiffness between these two endmembers (gray bonds in Figure 1c). In Figure 1c, the red bonds represent the weakest, most damaged material (the preexisting healed faults and distributed damage) and the blue bonds represent the strongest material (off the preexisting faults and damage). The red bonds connect the damaged particles, and the blue bonds connect the intact particles. The gray bonds connect damaged and intact particle pairs. We carefully calibrate the microparameters of these three sets of bonds in order to identify a set of microparameters that produces the macroscopic mechanical behavior of relatively intact granite, and more damaged fault zone material (Text S1 in Supporting Information S1). To achieve the loading conditions of a shear zone, we apply a constant normal stress on the top (at y position zero) and bottom (at y position 40 km) walls, and then apply a constant shear velocity to these walls (Figure S2 in Supporting Information S1). We move the top wall to the right and the bottom wall to the left. The dextral shear sense of the loading conditions produces restraining and releasing step over configurations when $y > 0$ and $y < 0$, respectively. Text S1, Figure S1, and Figure S2 in Supporting Information S1 describe additional details of the model set up.

4. Results

4.1. Macroscopic Mechanical Evolution and Fracture Development

The evolving macroscopic stress conditions and fracture geometry are closely linked to each other in these simulations (Figure 2). We examine this evolution in a model with an intermediate level of damage, $n = 1,000$, in a releasing step over geometry, $y = -2$ km. The relationship between fracture network growth and macroscopic stress of this model match this relationship in models with other fault geometries and levels of damage (e.g., Movies S1–S6 in Supporting Information S1). The applied shear velocity loading first increases the shear force acting on the top and bottom of the model, F_s, at a relatively constant rate. F_s is the sum of the shear forces acting on the top and bottom walls of the model. During this early stage of increasing F_s, between steps #1–8 in Figure 2, fractures develop along the preexisting faults, as well as throughout the system. As the change in F_s relative to the model timestep begins to decrease near step #9, fractures start to develop from the tips of the preexisting faults.
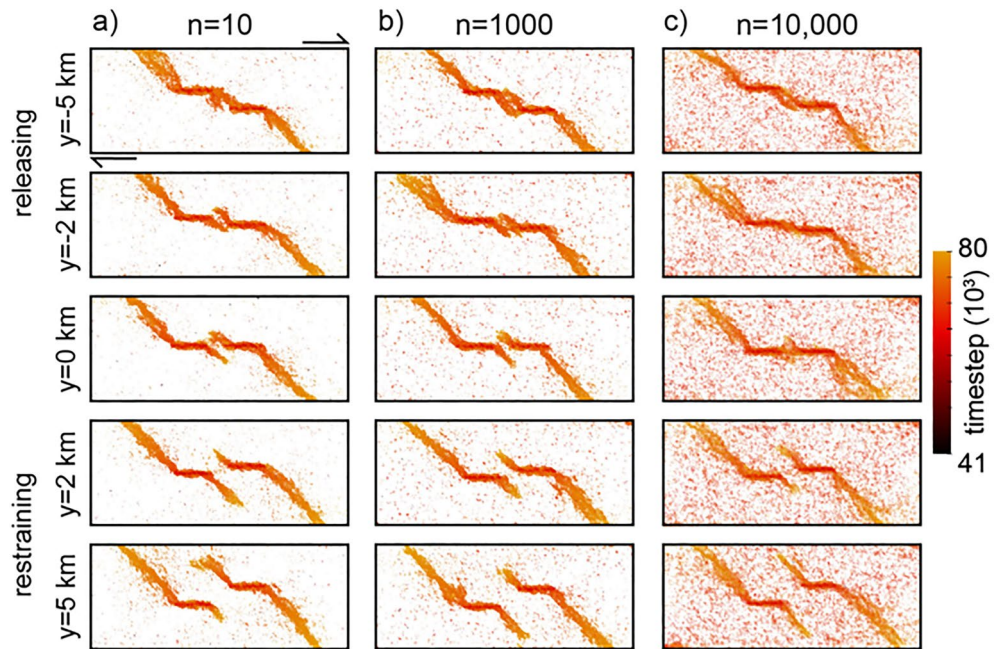
Figure 3. Fault geometry at the end of the simulation, before the faults begin to interact with the model boundaries, for models with low (a) $n = 10$, intermediate (b) $n = 1,000$, and high (c) $n = 10,000$ amounts of preexisting damage. The color of the fractures indicates the timestep when they developed.

Then, F_s decreases while the new faults propagate at oblique orientations from the preexisting faults, toward the upper left and lower right of the model, and toward the other preexisting fault within the center of the model. Toward the end of the simulation, F_s increases as the tips of the faults begin to interact with the model boundaries.

Next, we examine the fault geometries of the models with all of the tested levels of damage and fault configurations (Figure 3). The quadrants of varying compressive stresses that develop near the fault tips control the resulting fault geometry. Under the applied right lateral shear velocity loading conditions, lower compressive stresses develop at the upper left and lower right tips of the faults. Depending on the fault configuration and amount of preexisting damage, these local stress conditions either promote or hinder linkage of the faults in the center of the model. In the releasing step over configurations, $y < 0$, fault development from the lower right tip of the leftmost fault, and upper left tip of the rightmost fault, allow the faults to hard link, that is, one fault segment connects to another segment. In the restraining step over configurations, $y > 0$, these local stress conditions do not produce direct linkage of the faults within the center of the model. Instead, the new fault segments in the center of the model grow away from the other neighboring fault tip. Although these faults do not hard link to each other, their interaction may produce soft linkage, in which nearby faults perturb the slip distributions on neighboring faults without directly linking with them. In subsequent sections, we examine the off-fault velocity and strain distributions to identify soft linkage.

With increasing preexisting damage, n, the fault networks appear more diffusely distributed, and thus less distinguishable from the surrounding relatively more intact host rock (Figure 3). For example, the new fault segments at the outer edges of the models appear to be wider in the models with $n = 10,000$ than in the models with less damage. The level of damage also controls the fault geometry within the center of the model. In models with less damage, $n < 10,000$, the faults between the coplanar preexisting faults ($y = 0$) do not appear to hard link by the end of the simulation. In contrast, in the models with more damage, the two preexisting faults hard link. The more pervasive host rock damage in this model facilitated fault linkage.

4.2. Identifying Precursors in the Velocity Fields

To identify precursory signals of deformation in the simulations, we examine one-dimensional transects of the velocity field along both faults, similar to fault slip distributions measured in the field. The velocity of the
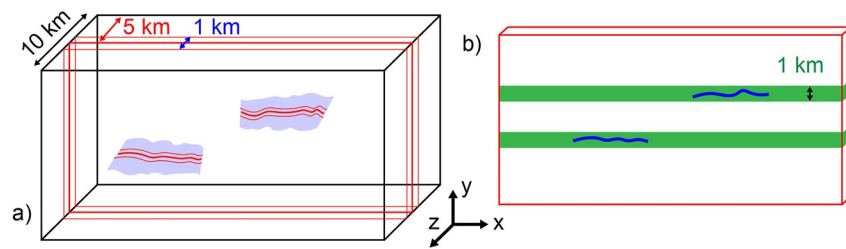
Figure 4. Extraction of the velocity field. (a) First, we take a 1 km wide two-dimensional slice of the velocity field at the center of the model at $z = 5$ km, throughout the x-y plane. (b) Then, we take one-dimensional transects that are 1 km wide of the velocity field along the y-position of the preexisting faults (green). To derive a cumulative representation of the velocity field along both faults (blue), we sum the velocity components and the velocity magnitude from the two transects at each x-position across the model width.

particles is equal to their displacement divided by the time step, and is thus representative of the local slip rate. Previous work has measured slip along neighboring faults to identify when such faults begin to perturb each others' slip distribution, and thus soft link (Peacock & Sanderson, 1991; Trudgill & Cartwright, 1994). To find additional evidence of soft linkage, such analyses may also sum the slip distributions from individual faults in a network because the cumulative slip distribution of two or more interacting, but unlinked, faults may produce an elliptical or bell-shaped slip distribution similar to the distribution measured along one fault (e.g., Mansfield & Cartwright, 2001). Thus, one characteristic that is indicative of fault interaction is the evolving cumulative slip distribution of multiple faults in a network.

4.2.1. Extracting Cumulative Transects of the Velocity Field

To estimate the cumulative slip distribution along the faults, we first subdivide the model domain into a grid of cubes with side lengths of one km, the radius of the largest particle. We then calculate the three means of the three components of the velocity vector of all the particles in a given cube at each model timestep. This cube size ensures that the extracted grid of velocity measurements is not governed by the anomalous velocity of one or two particles, and instead allows each cube to represent several tens of particles. We then take a two-dimensional cross section of the three-dimensional grid of cubes at the center of the model, $z = 5$ km, which is one km wide in the z direction, and extends throughout the x-y plane (Figure 4a). We extract one-dimensional transects of this two-dimensional cross section at the two vertical (y-direction) positions of the faults, across the x-axis of the model, at each model timestep (Figure 4b). In the following analysis, we first focus on the magnitude of the three-dimensional velocity vector, and later examine the individual components of the velocity vector. In all cases, we report the sum of the two transects along the y-positions of the faults, so that the resulting transect is the cumulative distribution across both faults. We consider the absolute value of the velocity components in order to directly compare the right-lateral and upward motion in the top portion of the model, and left-lateral and downward motion in the bottom portion. To compare the evolution of the velocity distributions through time, we report the velocity magnitude, and each of the velocity components, at each x-position in the transect normalized by the maximum velocity of that timestep. Without this normalization, the higher velocities at the end of the simulation obscure the patterns of the lower velocities earlier in the simulation. This procedure thus provides a timeseries of normalized cumulative velocity magnitude (or individual velocity components) transects across both faults throughout the simulations.

Examining the timeseries of the velocity magnitude transects suggests that the models host distributed deformation outside the preexisting healed faults, both before and after the faults break and slip (Figure 5). Models with larger vertical spacing between the faults, $y = \pm 5$ km, produce the most pervasive elevated diffuse deformation prior to slip along the preexisting faults. In the several thousand timesteps before the preexisting faults develop, the velocity magnitudes persist at elevated levels across a wider zone in models with $y = 5$ km than in models with closer spacing between the faults. Models with closer spacing host more localized zones of higher velocities. These results agree with crustal observations that find a positive correlation between the complexity of a fault network and the proportion of off-fault deformation (e.g., Dolan & Haravitch, 2014).

The amount of preexisting diffuse damage modifies these trends. In models with lower levels of damage, $n < 10,000$, regions with elevated velocity generally span across the simulation, from 20 to 60 km along the x-axis,
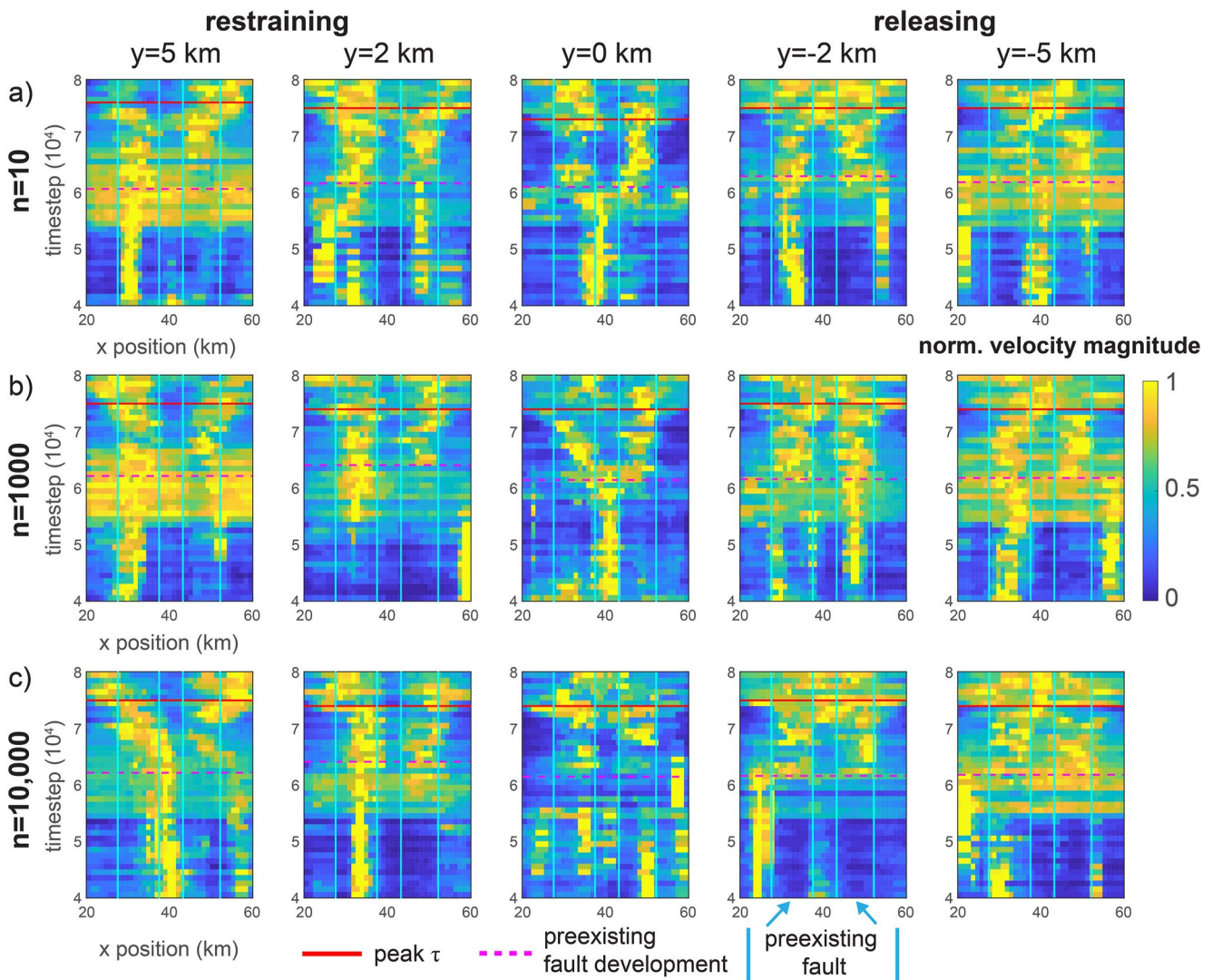
Figure 5. Transects of the cumulative normalized velocity magnitude along the *x*-axis at the *y*-positions of the two faults throughout the simulation for models with low (a) $n = 10$, intermediate (b) $n = 1,000$, and high (c) $n = 10,000$ amounts of preexisting damage. The columns show the velocity transects from different fault configurations, from the restraining, $y > 0$, to releasing, $y < 0$, step overs. Light blue vertical lines show the extent of the preexisting healed faults along the *x*-axis. Pink dashed line indicates when the two preexisting faults develop. Solid red line indicates when the models experience the maximum shear stress, and thus when new faults grow from the tips of the preexisting faults.

particularly when $y = 5$ km (Figures 5a and 5b). In models with $n = 10,000$, this pattern weakens (Figure 5c). Although the region experiences relatively higher velocities, these velocities are further from the maximum achieved at each timestep than in the models with lower preexisting damage. Thus, the existence of diffuse preexisting damage suppresses the pattern of higher velocities across the width of the model before the preexisting faults break and develop.

When the faults have closer spacing, $y = 2$ km, the highest velocity magnitudes appear to occur within the regions that the preexisting faults ultimately occupy. When the faults are coplanar, and the models have lower amounts of preexisting damage, $n < 10,000$, the highest velocity magnitudes tend to occur between the two preexisting faults. However, when the models have higher damage, $n = 10,000$, such a region of elevated velocity magnitudes does not occur between the preexisting faults. Instead, regions with elevated velocity occur throughout the width of the model, and are not concentrated between the two faults.

Thus, both the initial fault configuration and the amount of preexisting damage control the velocity field surrounding the faults. Crustal systems with (a) weak faults relative to the surrounding host rock, (b) coplanar faults, and
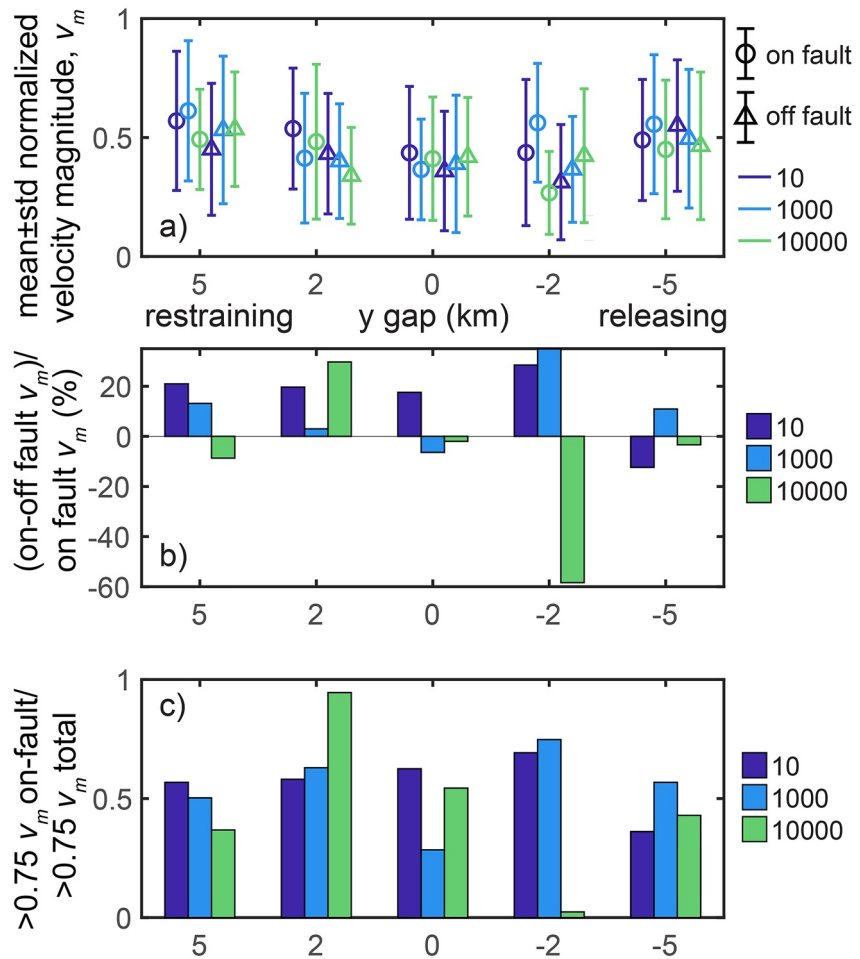
Figure 6. Differences in velocity magnitude within and outside the region that ultimately hosts the preexisting faults for all the fault configurations, and amounts of damage: (a) mean ± one standard deviation of the normalized velocity magnitude, v_m, within (on-fault, circles), and outside the future fault zone (off-fault, triangles), (b) difference between the mean v_m on- and off-fault divided by the on-fault v_m reported as a percentage, and (c) proportion of the highest normalized velocity magnitudes (>0.75) identified on-fault to the total amount identified throughout the system, p_{75}. The horizontal axis indicates the vertical spacing between the faults, the y gap. The colors of the lines indicate the different amounts of damage.

(c) steps with smaller separation distances may tend to produce precursory signals between the preexisting faults. However, in systems with relatively strong faults and/or more damaged host rock, the precursory signals may be more distributed across the network.

4.2.2. Comparing the Deformation On-Fault and Off-Fault

Qualitative observations of the timeseries of the velocity transects (Figure 5) indicate that the volume of rock outside the preexisting faults can host high magnitudes of velocity, as well as regions within the extent of the preexisting faults. To more systematically compare the amount of precursory deformation on- and off-fault, we compare the mean velocity magnitudes that occur within and outside the regions where the preexisting faults eventually form (Figure 6). In order to focus on precursory signals, we focus on the simulation time before the formation of the preexisting faults. In the following analysis, we refer to the statistics extracted from the regions in which the preexisting faults form as on-fault, and the remaining regions as off-fault. However, we note that these preexisting faults have not yet developed during the simulation time we examine in this analysis. The on-fault regions are within one km of the preexisting fault surface, and thus include both on-fault and damage zone bonds.

One may expect that the highest precursory velocities would develop in the region that ultimately forms the faults, rather than the off-fault zone. However, this localization may only occur in a very short time interval immediately prior to the main faulting event. Comparing the difference between the normalized velocity magnitudes, v_m, in

the on-fault and off-fault zones indicates that the ranges of the mean ± one standard deviation generally overlap for these zones (Figure 6a). Similarly, the difference between v_m in the on-fault and off-fault zones is generally <20% of the on-fault v_m, although one model has a difference of near 60% ($y = -2$ km, $n = 10,000$) (Figure 6b). This difference arises because the on-fault v_m is significantly lower than the off-fault v_m when $n = 10,000$ and $y = -2$ km. Contrary to the expectation of higher precursory velocities on-fault than off-fault, several models experience higher mean off-fault velocities than mean on-fault velocities, producing negative values in Figure 6b.

Increasing amounts of preexisting diffuse damage outside of the fault zones promote off-fault deformation. In particular, only one of the models with $n = 10$ has a higher mean off-fault velocity than on-fault velocity, whereas four of the models with $n = 10,000$ have higher mean off-fault velocities. Greater preexisting damage away from the preexisting faults produces stronger signals of precursory deformation off-fault. This result agrees with analyses of crustal fault systems that find that the proportion of off-fault deformation increases as the strength of the host rock decreases (e.g., Zinke et al., 2014).

To further quantify the partitioning of precursory signals on-fault and off-fault, we examine which regions experience the highest normalized velocity magnitudes (>0.75) (Figure 6c). We report the proportion, p_{75}, of the fault length that experiences >0.75 normalized velocity magnitude, relative to the proportion of the total length that experiences magnitudes greater than this threshold. Increasing amounts of damage increases the variability of this proportion, p_{75}. For models with $n = 10,000$ and $y = -2$ to 2 km, for example, the range of p_{75} is close to the maximum possible range, from zero to one. This range indicates that the strongest precursory signals may occur either entirely within ($y = 2$) or outside ($y = -2$) the preexisting fault zone, depending on whether the fault configuration is a releasing or restraining step over.

At lower amounts of damage, the range of p_{75} is more consistent across the different fault geometries. The average p_{75} across the different fault geometries is 0.56 and 0.54, for $n = 10$ and $n = 1,000$, respectively. Thus, the strongest precursory signals of deformation are similarly likely to be found within and outside of the regions that host the preexisting faults. In contrast to the expectation that the strongest precursory movement should occur within the eventual fault zone, the models reveal a similar likelihood of identification outside the future fault zone. Varying the threshold used to identify the proportion of high velocity magnitudes on-fault from 0.70 to 0.95 does not change this conclusion (Figure S3 in Supporting Information S1). Examining how p_{75} varies through time does not reveal systematic changes toward failure (Figure S4 in Supporting Information S1). This proportion increases toward failure in some models, and decreases or remains at similar values in others. Thus, contrary to the idea that deformation progressively localizes toward the preexisting fault, the models indicate that in systems with several individual fault segments, precursory deformation remains spread pervasively throughout the fault network and surrounding crustal volume, and does not systematically localize toward fault reactivation.

4.2.3. Examining the Size and Temporal Continuity of Regions of Elevated Deformation

To assess which velocity component may host the most valuable precursory signals, we now examine the size of the continuous regions of elevated velocities in the timeseries of transects, and how these sizes differ between the velocity components (Figures 7 and 8). The size of the continuous regions with higher velocities, in space and time, may suggest which velocity component provides the most detectable signals. For example, if a fault system hosts elevated velocity at one particular location along the fault strike at a particular time, and then hosts similarly high velocity at the same location at later times, this reoccurring elevated velocity may be easier to detect than if such elevated velocities change their positions. When higher velocities persist in the same position, the size of the continuous region of higher velocities will be larger than if the higher velocities shift positions throughout time.

The imposed right-lateral shear loading parallel to the x-axis suggests that the models may produce larger continuous regions of the x-component of the velocity vector, v_x, than other two components, v_y and v_z. However, fault networks with step overs also experience uplift and subsidence, and fault perpendicular motion (e.g., McClay & Bonora, 2001). These types of deformation could produce relatively larger continuous motion with elevated v_z (uplift/subsidence), and v_y (fault perpendicular motion).

To compare the sizes of regions with continuous precursory deformation, we create a binary two-dimensional map of the velocity timeseries for each velocity component in which normalized velocities >0.75 are labeled one, and velocities <0.75 are labeled zero (Figure 7). We only extract this map from the model time before the preexisting faults slip, in order to focus on precursory signals. We identify the individual connected clusters of the binary space-time maps using 8-fold connectivity, the most conservative type of connectivity in two dimensions.
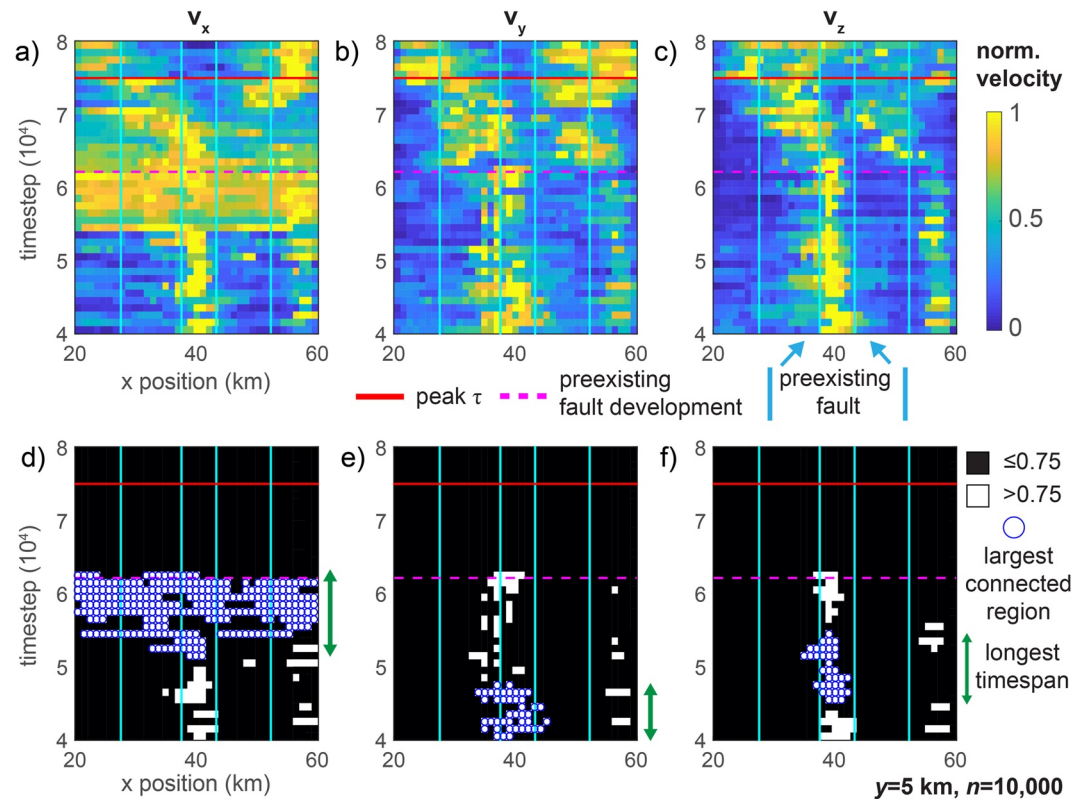
Figure 7. Method of identifying continuous regions of higher velocities for the model with $y = 5$ km and $n = 10{,}000$, and each velocity component: v_x (a and d), v_y (b and e), and v_z (c and f). We first use the normalized velocity transect timeseries (a–c) to produce a binary field in which ones represent where the normalized velocity components are >0.75 (d–f). Then, we identify the connected components in this field using 8-fold connectivity. We next identify the cluster of high velocities that has the largest area (blue circles), and the longest length in the time dimension (green line). In this example, the largest cluster also has the longest time span, but this result is not required, that is, the cluster with the largest area may not be the cluster with the longest timespan.

This connectivity requires that both the edges and the corners of pixels must be touching in order to be identified as connected. The identified clusters have one dimension in the model time and another dimension in the model length-scale (km). To compare the ability of each component to provide valuable precursory information, we measure the area and length along the time-axis of the clusters. Larger areas indicate velocity components with larger continuous regions of elevated velocities, in both space and time. Longer time spans indicate velocity components with more persistent locations of elevated velocities, in only the time dimension. Identifying the velocity component with the largest area of continuous higher velocities, and the longest time span, may suggest which velocity component can provide the most detectable precursory activity. In some cases, the cluster with the largest area may also have the longest timespan (e.g., Figure 7), however, this condition is not required.

To compare the properties of continuous regions of higher velocity magnitudes, we report the difference between the property (area ΔA, or timespan Δt) of the high magnitudes of the v_x and v_y, or the v_x and v_z divided by the maximum of v_x and the other strain component. The imposed shear displacement loading parallel to the x-axis suggests that v_x may form larger areas and timespans than the other components. Thus, we report the difference in the property as $v_x - v_y$ or $v_x - v_z$. Positive values indicate that v_x forms larger areas or timespans than either v_y or v_z for a given model. We first focus on results using a threshold of 0.75 to extract the continuous regions of high velocity, and describe the results using different thresholds in Supporting Information S1 (Figure S5 and S6).

Comparing the maximum areas of the continuous regions of higher velocities (>0.75) for each velocity component indicates that the fault configuration influences which velocity component has the largest area (Figure 8). In models with larger steps, v_x has larger maximum areas than the other components, producing positive ΔA. The broad regions of elevated velocity that extend across the model width (e.g., Figure 5) produce the high areas
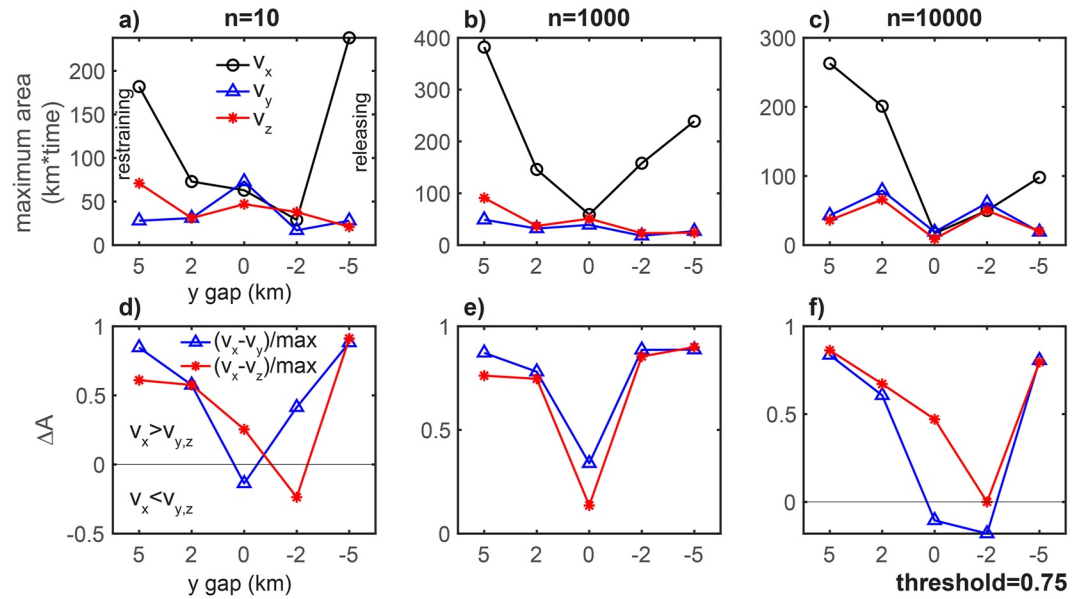
Figure 8. Identifying the dominant velocity component using the maximum area of continuous regions of higher velocity (>0.75 of the normalized velocity) from timeseries of models with different levels of damage: $n = 10$ (a and d), $n = 1,000$ (b and e), and $n = 10,000$ (c and f). (a–c) Maximum area of the continuous regions. Black, blue, and red lines indicate the areas for the regions of the v_x, v_y, and v_z, respectively. (d–f) Difference between the areas of v_x and the other two components, ΔA. Red and blue lines indicate the difference between v_x and v_z, and v_x and v_y, respectively. The horizontal axis indicates the step over distance between the faults, the y gap. For the models with larger step over distances, v_x forms larger continuous regions of higher velocities in the model time before the preexisting faults slip than the other two components. For models with coplanar faults and smaller step over distances, the three velocity components form similarly large continuous regions, producing low positive or negative ΔA.

(Figure 8). In models with coplanar faults and smaller steps, the maximum areas are similar for the three components, producing lower positive ΔA, and sometimes negative ΔA.

The maximum timespans of the continuous regions of elevated velocities generally indicate longer timespans for v_x than the other components (Figure 9), producing positive Δt. However, for some models, the three velocity components form regions of continuous elevated velocity that span similar lengths of time, producing low positive and sometimes negative Δt. The normalized difference between the timespans of v_x and v_z is negative or near zero for about half of the models, indicating the similar continuity of these velocity components. The normalized difference between the timespans of v_x and v_y is near zero for four of the fifteen models. Although v_x often forms longer timespans, some models experience similar or slightly longer timespans for the other components, and particularly v_z.

In summary, higher amounts of preexisting diffuse damage tend to favor precursory deformation in the y and z-directions, as uplift and subsidence, and fault perpendicular motion. Lower amounts of damage produce regions of elevated velocity parallel to the faults that are larger in area and longer in time than the other velocity components. Thus, in systems with relatively weak faults, with lower uniaxial compressive strength and Young's modulus, crustal monitoring efforts may focus on the deformation component that is parallel to the faults, but in general it is useful to analyze the other components of deformation as well.

The previous analyses quantified the geometric properties of the continuous regions of elevated velocity throughout the entire simulation time preceding slip on the healed faults. However, these geometric properties could evolve in the time leading to slip. Thus, we now compare the maximum areas and timespans of the velocity components at different time intervals leading to fault reactivation (Figure 10). We calculate the areas and timespans for each velocity component in four time steps from when the applied shear velocity loading starts to when the faults slip, at 0%–25%, 25%–50%, 50%–75%, and 75%–100% of the timestep when the faults slip. We
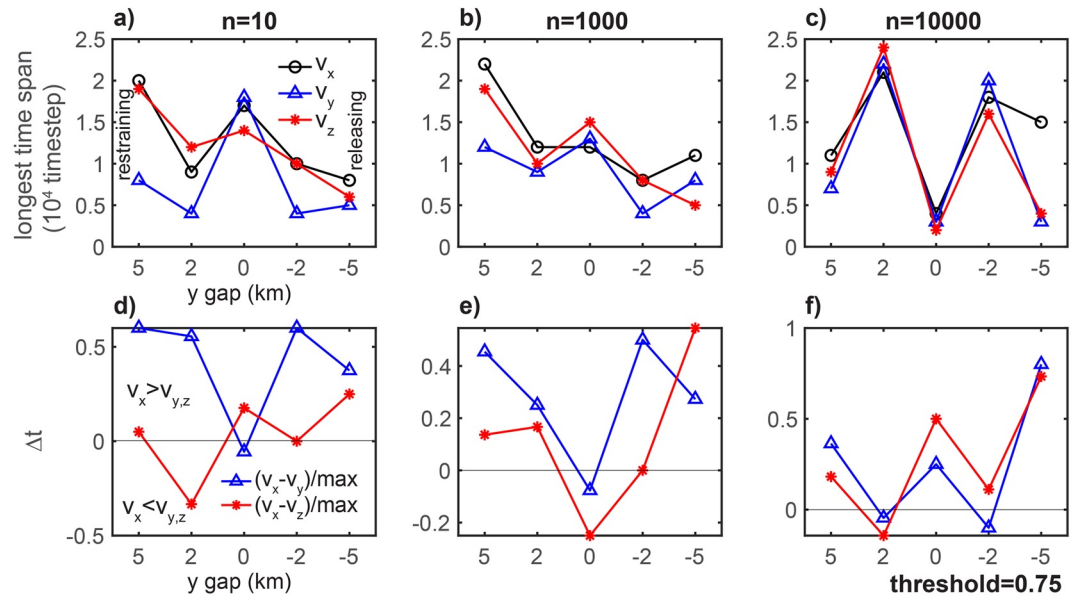
Figure 9. Identifying the dominant velocity component using the maximum timespan of continuous regions of higher velocity (>0.75 of the normalized velocity) from timeseries of models with different levels of damage: $n = 10$ (a and d), $n = 1,000$ (b and e), and $n = 10,000$ (c and f). (a–c) Maximum timespan of the continuous regions. Black, blue, and red lines indicate the areas for the regions of the v_x, v_y, and v_z, respectively. (d–f) Difference between the timespan of v_x and the other two components, Δt. Red and blue lines indicate the difference between v_x and v_z, and v_x and v_y, respectively. The horizontal axis indicates the step over distance between the faults, the y gap.

compare the areas and timespans of v_x to the other two components using the difference between v_x and the other component for the areas, ΔA, and timespans, Δt (e.g., Figure S6 in Supporting Information S1). More positive values indicate that v_x forms larger or longer continuous regions of elevated velocity than the other two components.
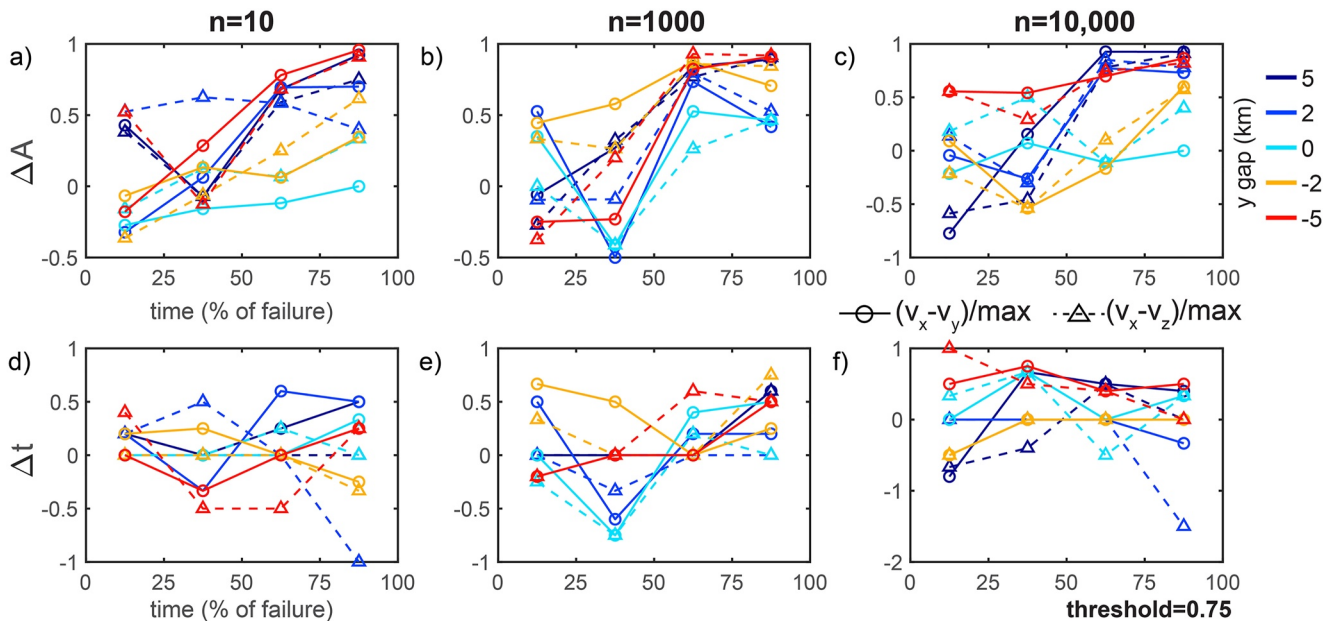

Figure 10. Temporal evolution of geometric properties of the velocity components for models with preexisting diffuse damage $n = 10$ (a and d), $n = 1,000$ (b and e), and $n = 10,000$ (c and f) and all of the fault configurations (colors) as the difference between the geometric property (top row, area, ΔA, or bottom row, timespan, Δt) of the high magnitudes (>0.75) of the v_x and v_y (circles and solid lines), or v_x and v_z (triangles and dashed lines) divided by the maximum of that property. Thus, positive values indicate when the timespan or area of v_x is larger than the other velocity component.

Examining the trends in ΔA indicates that ΔA increases toward fault reactivation (Figures 10a–10c) as v_x forms increasingly larger areas of elevated deformation compared to the other two components. The difference in the timespans of the velocity components do not evolve systematically toward failure (Figures 10d–10f). Thus, the velocity magnitude does not systematically localize to the preexisting fault (Figure S4 in Supporting Information S1), and the timespans of the velocity components do not increase toward failure (Figures 4d–4f); however, the regions with elevated v_x increase in area as the system approaches the reactivation of the preexisting faults (Figures 10a–10c).

4.3. Identifying Precursors in the Strain Fields

Laboratory observations indicate that low porosity crystalline rocks dilate preceding macroscopic failure under triaxial compression (Brace, 1978). Similarly, machine-learning analyses indicate that the dilative component of the strain field provides more valuable information about the proximity of failure than the contractive or shear strain components in triaxial compression experiments (e.g., McBeck, Aiken et al., 2020). To constrain the ability of these strain components to provide information about the proximity of failure in shear zones with step overs, we examine the timeseries of transects of these components derived with a similar method as the velocity transects (e.g., Figure 5). However, instead of extracting the strain components from the two-dimensional slice of the velocities, we extract a three-dimensional volume of the velocity components so that we may calculate the three-dimensional strain tensor throughout the system. This three-dimensional volume spans the area of the x-y plane that the two-dimensional slices include, and also extends across the full thickness of the model along the z-axis (e.g., Figure 4).

We examine the first invariant of the strain tensor, I_1, and the second invariant of the deviatoric strain tensor, J_2:

$$I_1 = \varepsilon_{xx} + \varepsilon_{yy} + \varepsilon_{zz} \tag{1}$$

$$J_2 = \frac{1}{6}\left[(\varepsilon_{xx} - \varepsilon_{yy})^2 + (\varepsilon_{yy} - \varepsilon_{zz})^2 + (\varepsilon_{zz} - \varepsilon_{xx})^2\right] + \varepsilon_{xy}^2 + \varepsilon_{yz}^2 + \varepsilon_{zx}^2 \tag{2}$$

The value of I_1 quantifies the volumetric strain, while J_2 quantifies the deviatoric or shear strain. For example, the von Mises yield criterion uses J_2 to determine the stress conditions at which a material will fail. We sample the I_1 and J_2 fields at the same positions of the one-dimensional transects that we used to sample the velocity components, at $z = 5$ km and at the y-position of both faults (e.g., Figure 4). From the resulting timeseries of strain transects, we normalize the absolute value of the strains by the maximum strain at each timestep. First, we examine the timeseries of the contractive and dilative components of I_1, that is, the negative and positive values of I_1, as well as the absolute values of I_1 and J_2 (Figure 11). At the positions in the timeseries of contraction (negative I_1) that do not host contraction, where I_1 is positive, we report these values of contraction as zero (Figure 11). Thus, only the regions that host contraction have non-zero values in the first column of Figure 11. This approach is also used for the dilation timeseries, so the plots of contraction and dilation are approximately inverse images of each other.

The patterns of the shear strain, volumetric strain, and dilation fields after the peak macroscopic shear stress confirm our earlier qualitative observations of fracture network development, and the corresponding influence of preexisting damage on this development for models with coplanar faults, $y = 0$ (Figure 3). The fracture networks shown in Figure 3 suggest that the faults do not link when the models have damage $n < 10{,}000$, and do link when $n = 10{,}000$. The timeseries of the strain fields similarly suggest linkage of the faults only when $n = 10{,}000$, and not with lower levels of damage (Figure 11). In particular, after the peak macroscopic shear stress, and thus the development of the new faults, higher magnitudes of volumetric strain, dilation, and shear strain concentrate within the region of the preexisting faults (Figure 11, Figure S7 and Figure S8 in Supporting Information S1). In the models with $n = 10{,}000$, higher magnitudes of this strain span the preexisting faults, and the region between them. In models with lower amounts of damage, $n = 10$ and $1{,}000$, in contrast, higher magnitudes of strain do not develop between the preexisting faults.

Next, we compare the areas and timespans of the continuous regions with the highest volumetric and shear strain magnitudes, following the same method as the velocities (e.g., Figure 7). We only compare the volumetric strain and the shear strain, and not the dilation and contraction. Direct comparison of the areas of high magnitudes of strain in the dilation and shear strain field, for example, is hindered by the fact that the dilation timeseries only
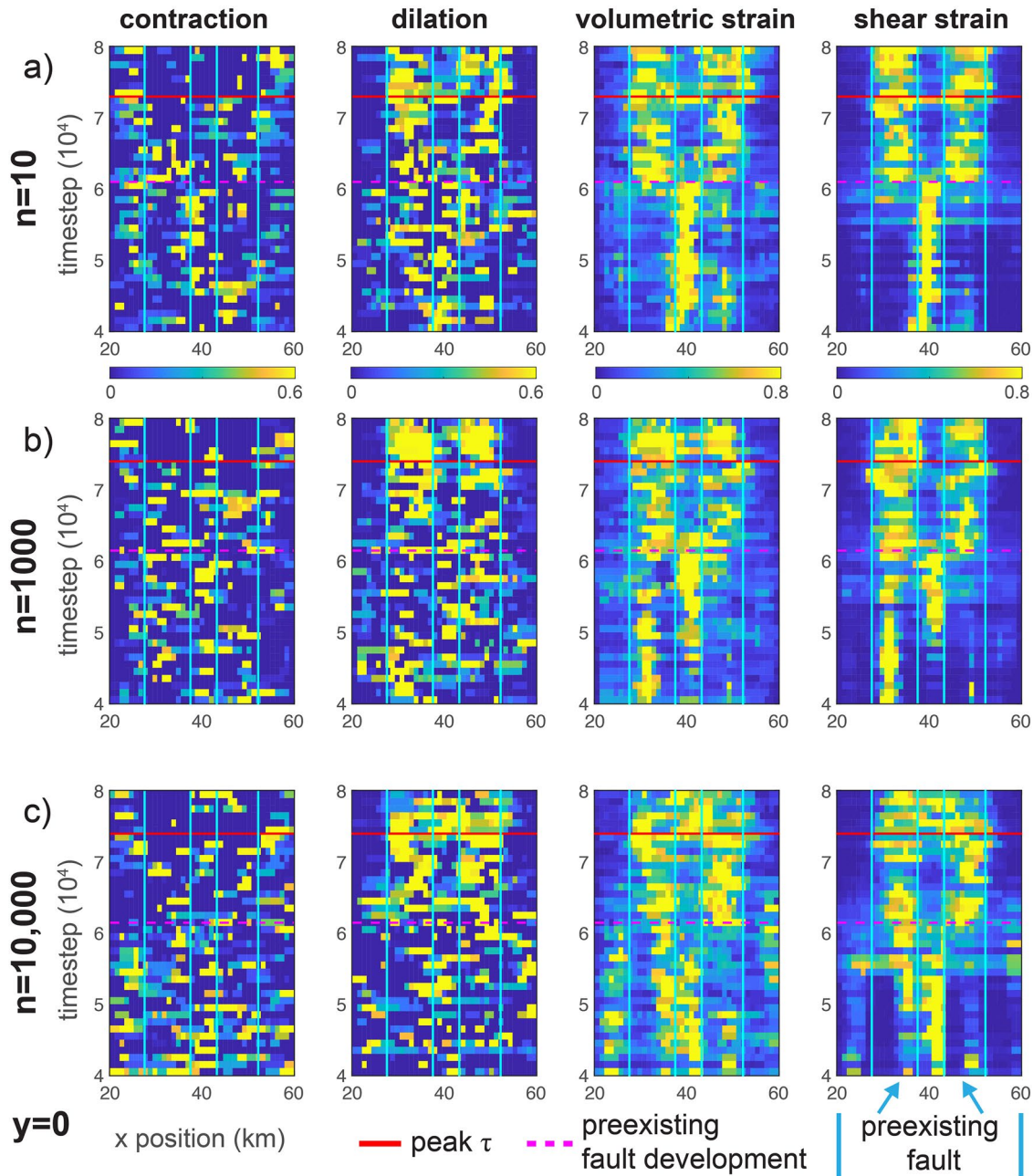
Figure 11. Transects of the normalized absolute value of the contraction, $I_1 < 0$, dilation, $I_1 > 0$, volumetric strain, I_1, and shear strain, J_2, along the x-axis at the y-position of the preexisting faults throughout the simulation for models with low, $n = 10$ (a), intermediate, $n = 1,000$ (b), and higher, $n = 10,000$ (c), amounts of preexisting diffuse damage, and $y = 0$ km. Light blue vertical lines show the extent of the faults along the x-axis. Pink dashed line indicates when the two preexisting faults develop. Solid red line indicates when the models experience the maximum shear stress, and thus when new faults grow from the tips of the preexisting faults. The highest magnitudes of the dilation and contraction appear randomly distributed throughout the model preceding fault development. In contrast, the volumetric and shear strain fields develop patterns more similar to the velocity magnitude, consisting of elevated magnitudes at persistent locations throughout time.

covers a small portion of the total shear strain timeseries. Because both contraction and dilation occur within the model with similar proportions, the maximum possible area of a continuous region of higher shear strain is larger than that possible area of the dilation.

We first calculate the maximum areas of the continuous regions of normalized shear strain that is greater than 0.75, $A_{75}^{J_2}$, and the normalized volumetric strain that is greater than 0.75, $A_{75}^{I_1}$. Similarly, we calculate the longest timespans of these continuous regions of the shear strain, $t_{75}^{J_2}$, and volumetric strain, $t_{75}^{I_1}$. We report the difference
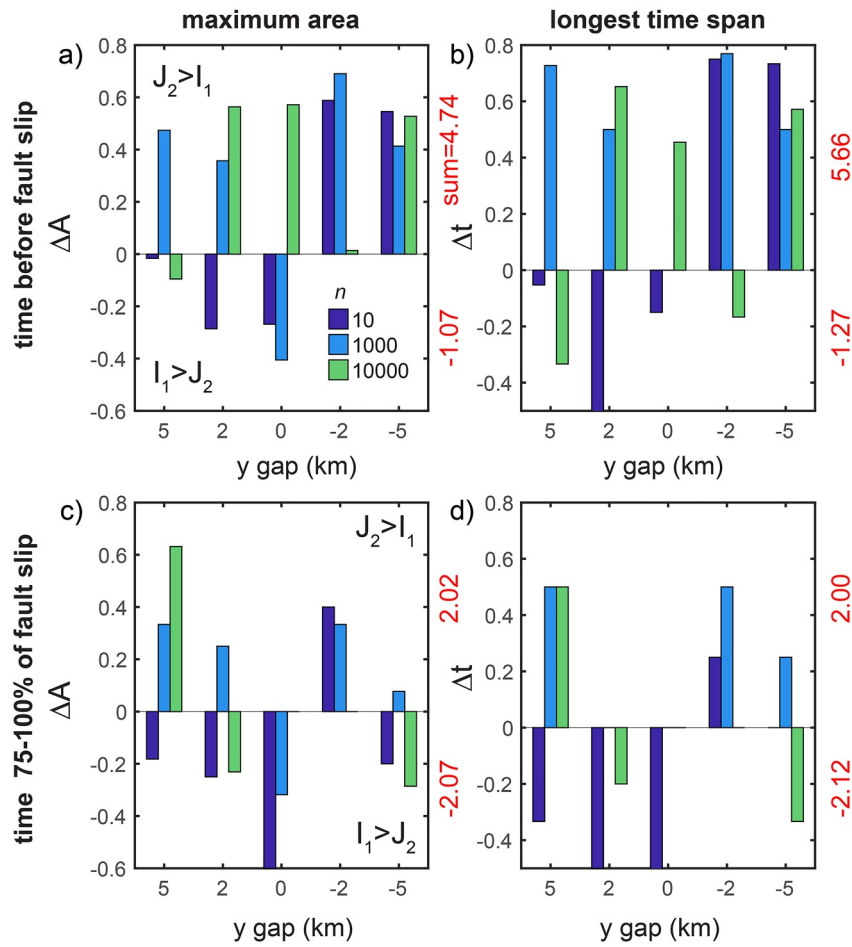
Figure 12. Identifying the strain component that may provide the most valuable precursory information throughout the full simulation time before slip on the preexisting faults (a and b) and in the timesteps near failure, 75%–100% of the model time before fault slip (c and d). (a and c) Difference in the maximum areas of the continuous regions of higher normalized shear strain (>0.75), $A_{75}^{J_2}$, and volumetric strain, $A_{75}^{I_1}$, normalized by the maximum of $A_{75}^{J_2}$ and $A_{75}^{I_1}$, ΔA. (b and d) Difference in the longest timespans of the continuous regions of higher normalized shear strain (>0.75), $t_{75}^{J_2}$, and volumetric strain, $t_{75}^{I_1}$, normalized by the maximum of $t_{75}^{J_2}$ and $t_{75}^{I_1}$, Δt. The positive values are divided by the geometric property of the volumetric strain, I_1, area or time span, and the negative values are divided by the geometric property of the shear strain, J_2. For example, positive $\Delta A = \left(A_{75}^{J_2} - A_{75}^{I_1} \right) / A_{75}^{I_1}$, and negative $\Delta A = \left(A_{75}^{J_2} - A_{75}^{I_1} \right) / A_{75}^{J_2}$. The red numbers to the right of each plot show the sum across all of the models with positive ΔA, and negative ΔA, (a and c), and positive Δt, and negative Δt (b and d).

in the areas, $\Delta A = A_{75}^{J_2} - A_{75}^{I_1}$ divided by the maximum of $A_{75}^{I_1}$ and $A_{75}^{J_2}$. Similarly, we report the difference in the timespans, $\Delta t = t_{75}^{J_2} - t_{75}^{I_1}$ divided by the maximum of $t_{75}^{I_1}$ and $t_{75}^{J_2}$. Thus, when ΔA and Δt are positive, the shear strain timeseries produce larger regions with longer timespans than the volumetric strain timeseries. Because precursory signals may evolve toward failure, we calculate ΔA and Δt throughout the complete simulation time leading up to the reactivation of the preexisting faults (Figures 12a and 12b), and during the model time immediately preceding failure (Figures 12c and 12d), when the model timestep is 75%–100% of the timestep when the faults slip.

Throughout the full simulation time preceding fault reactivation, the generally positive values of ΔA indicate that the continuous regions of higher shear strain tend to occupy larger areas than the volumetric strain (Figure 12a). Similarly, the majority of the models host continuous regions of high shear strain that span longer time intervals than the volumetric strain, producing positive Δt (Figure 12b). Moreover, the positive values of ΔA and Δt tend to be larger than the negative values of ΔA and Δt. The sum of the positive ΔA across all of the models is 4.74, while the negative ΔA sum is −1.07. Similarly, the sum of the positive Δt is 5.66, while the negative Δt sum is −1.27. Thus, even when the volumetric strain occupies larger areas or longer timespans than the shear strain, the

difference between the two components is smaller than when the shear strain occupies larger areas or timespans. The models that tend to produce negative ΔA and Δt include restraining step overs. In summary, the shear strain fields tend to involve larger regions of elevated strain that span longer time intervals than the volumetric strain for the full simulation time leading to fault reactivation.

However, the relative dominance of the shear strain evolves toward failure (Figures 12c and 12d). Whereas the positive values of ΔA and Δt tend to be larger than the negative values of ΔA and Δt for the full simulation time (Figures 12a and 12b), the positive and negative values of ΔA and Δt are more similar to each other immediately preceding failure. In particular, for the simulation time 75%–100% of the model timestep before fault reactivation, the sum of the positive ΔA across all of the models is 2.02, and the negative ΔA sum is −2.07. The sum of the positive Δt is 2.00, and the negative Δt sum is −2.12. Varying the threshold used to extract the regions of higher strain does not change these key conclusions (Figure S9 in Supporting Information S1).

5. Discussion

To facilitate the identification of accelerating geophysical signals prior to fault slip, we examined the evolving three-dimensional deformation fields surrounding releasing and restraining step overs preceding slip along healed faults in discrete element method models. We assume that the locations and style of the precursors identified in the models may be similar to corresponding phenomena in kilometer-scale crustal fault networks. The properties of the precursory deformation identified in the models may be the most applicable to crustal scale systems with similar geometries to the numerical models: with releasing and restraining step overs including faults of similar lengths that are underlapping by half of a fault length, and separated in the fault perpendicular direction by up to half of the length of the faults.

5.1. Locations of Precursors: Comparing the Magnitude of On-Fault and Off-Fault Deformation

The models indicate that both the initial fault configuration and amount of preexisting host rock damage influence where the strongest deformation occurs prior to slip on healed faults. At the lowest amounts of damage, models with larger steps, of one fault half-length between the faults, produce the widest extent of elevated deformation (i.e., normalized particle velocity magnitude >0.70–0.95) across the model prior to slip (e.g., Figure 5). Models with coplanar faults produce more localized regions of elevated deformation, in general between the healed faults.

These results agree with geodetic and field observations that indicate that the structural maturity of a fault system influences the amount of off-fault deformation. For example, structurally immature faults with more complex geometries hosted only about 50%–60% of the total slip of six $M_w \geq 7.1$ strike-slip earthquakes, whereas more mature faults with more planar geometries hosted 85%–95% of the slip (Dolan & Haravitch, 2014). Similarly, COSI-Corr correlation of aerial photographs before and after the 1992 M_w 7.3 Landers earthquake suggest that 46% of the total surface deformation occurred off-fault, and that the magnitude and width of the distributed deformation was the largest in parts of the fault network with more complex fault geometries, such as step overs and bends (Milliner et al., 2015).

Thus, several geophysical observations and our numerical models suggest that as fault networks evolve from more complex geometries toward more structurally simple, coplanar systems, they tend to host an increasing proportion of the total deformation on-fault (e.g., Figure 13a). This evolution may occur because fault networks evolve to optimize the total energy expended in the system (e.g., Cooke & Madden, 2014). As faults grow and slip, the amount of energy consumed in frictional work increases (e.g., Del Castello & Cooke, 2007; McBeck et al., 2018). If this growth decreases the internal work done in diffuse, off-fault deformation by a greater magnitude than the increase in frictional work, the total energy expended in the system may decrease, producing a more efficient system. Thus, the observed progression from complex to simple fault geometries, paired with the reduction of off-fault deformation, may occur because fault networks evolve toward energetic efficiency.

Increasing the amount of preexisting host rock diffuse damage changes the observed location of precursors, and the corresponding link between the fault configuration and the extent of deformation. For the coplanar models, increasing the amount of damage from $n = 1,000$ to $n = 10,000$ removes the persistent pattern of elevated deformation between the two faults. Instead of remaining localized between the coplanar faults, the regions that host the most deformation vary through time. For models with the largest tested steps, increasing the amount of
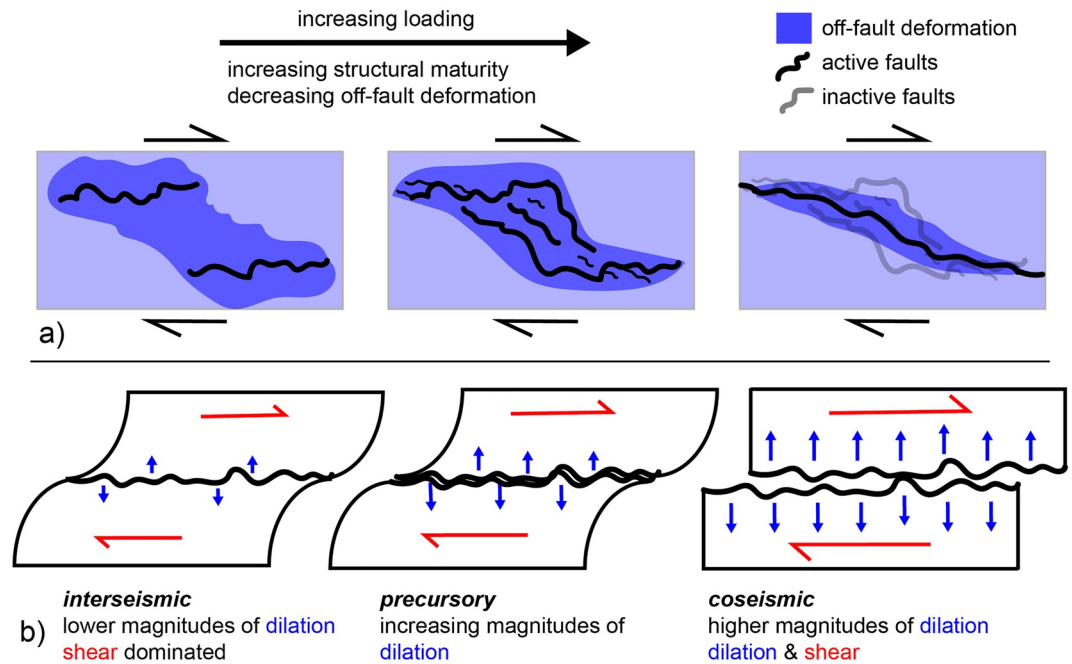
Figure 13. (a) Sketch of the evolution of structural maturity and off-fault deformation in a step over. Early in step over development, a broad region of elevated off-fault deformation may develop between adjacent fault segments (e.g., Cooke et al., 2013). With increasing loading, linking fault segments propagate between the adjacent segments. With further displacement, the fault network may localize as some fault segments become inactive and the network evolves to optimize the overall efficiency of the system. (b) The varying proportions of shear and dilation throughout the seismic cycle. In the interseismic period, the strain field is dominated by shear. During the precursory and coseismic phases, higher magnitudes of dilation may develop to enable the slip along rough surfaces.

diffuse damage from $n = 1,000$ to $n = 10,000$ only weakens the pattern of elevated deformation across the width of the model, but does not remove it. The observed elevated deformation outside of the regions that host the healed faults produces higher mean particle velocity magnitudes in this region, rather than inside the future fault zone (Figure 6). Similarly, the highest velocity magnitudes of a given model timestep, >0.75 of the normalized velocity, occur off-fault and on-fault with similar frequency in several models. The models reveal that the presence of distributed damage, or decreasing the difference in strength between the host rock and the healed fault zone, produces stronger signals of precursory off-fault deformation (Figure 6). The evolution of the proportion of off-fault deformation does not evolve systematically toward fault reactivation across all of the models: in some models, the proportion of off-fault deformation decreases toward fault reactivation, and in others it increases (Figure S4 in Supporting Information S1).

This link between the amount of host rock damage and off-fault deformation agrees with field observations that find a correlation between the type of near-surface materials and amount of off-fault deformation (e.g., Milliner et al., 2015; Rockwell et al., 2002; Zinke et al., 2014). For example, observations of linear features offset in the M_w 7.4 August and M_w 7.1 November 1999 North Anatolian fault earthquakes indicate that off-fault deformation ranged from zero to 40% of the total slip, and that significant distributed off-fault deformation occurred in areas of alluvial fill (Rockwell et al., 2002). Similarly, COSI-Corr correlation of satellite imagery suggests that on average 45% of the surface displacement occurred off-fault in the 2013 M_w 7.7 Balochistan, Pakistan earthquake, and that more off-fault deformation occurred in younger and/or thicker sediments than bedrock and older sediments (Zinke et al., 2014). In addition, observations of the surface displacement due to the 1,992 M_w 7.3 Landers earthquake indicate larger proportions of off-fault deformation in areas dominated by younger, alluvial deposits, than areas that include a mixture of these sediments and more intact bedrock (Milliner et al., 2015). However, the proportion of off-fault deformation in areas dominated by more intact bedrock yield similar magnitudes as the areas dominated by sediment (Milliner et al., 2015). This unexpected result may occur due to the influence of fault geometry on the proportion of off-fault deformation. These observations suggest that both the complexity of the fault geometry and the strength of the host rock relative to the fault core control the magnitude of off-fault

deformation. More complex fault geometries and weaker host rock promote more off-fault deformation than more planar fault geometries and stronger host rock. These observations agree with the results from our numerical models, which find greater magnitudes of off-fault deformation in models with larger steps, and in models with higher levels of diffuse damage.

These crustal observations focused on the deformation that occurred shortly before and after large earthquakes, rather than the deformation leading to the main event. In the models presented here, we are able to examine the deformation field preceding slip on the healed faults with fine temporal resolution. We find similar relationships between the relative proportion of off-fault deformation and fault complexity, and off-fault deformation and host rock strength, in the time span leading to slip on the healed faults as these relationships observed before and after crustal earthquakes. The similarity of these results suggest that these models of quasistatic fault development adequately simulate the processes that produce the observed partitioning of deformation on- and off-fault in the crust, similar to other discrete element method models (e.g., Blank & Morgan, 2019).

Due to the difference between the host rock strength and fault zone material, one may expect the strongest precursors to occur within the region that hosts the healed preexisting faults. Contrary to this expectation, the models indicate a similar likelihood of identification outside and within the future active fault zone (Figure 6; Figure S4 in Supporting Information S1). Crustal monitoring efforts may thus benefit from instrumenting regions of the crust not only near faults, but also at some distance from preexisting faults. In particular, fault systems with larger steps, of half of a fault length, and systems with more damaged crust, may produce regions with relatively strong precursors both within and outside the preexisting healed faults. The models suggest that these signals can occur up to one fault length outside the healed faults.

The locations of the identified precursory deformation may also shed light on the ability of earthquakes to rupture across step overs. Restraining, or contractive, step overs appear to arrest earthquake rupture at a smaller step distance than releasing, or dilative, step overs (e.g., Harris & Day, 1993; Wesnousky, 2006). The presence of off-fault damage between the steps may assist the ability of earthquakes to propagate across them. The weaker material, with lower uniaxial compressive strength and stiffness, may allow earthquake rupture to propagate through such weak barriers rather than through stronger material. Our numerical models show that the faults propagate toward each other and hard link when they are in a releasing step, but not in a restraining step (Figure 3). Recent numerical models that include dynamic rupture show that off-fault damage promotes earthquake triggering on faults in releasing step overs (Okubo et al., 2020). Although our simulations do not model earthquake rupture and coseismic deformation, they provide additional explanation of why ruptures can propagate across larger dilative steps than contractive steps, in particular, because diffuse off-fault deformation can influence the dynamics of earthquake rupture (e.g., Finzi & Langer, 2012; Lyakhovsky et al., 2001).

5.2. Style of Precursory Deformation

The models provide information about both the location of precursory deformation and the style of this deformation. The fault parallel velocity component, v_x, tends to form larger areas and longer timespans than the other two components (Figures 8 and 9). Moreover, the difference in the area of v_x and the other two components increases toward failure (Figure 10), suggesting the importance of tracking v_x in the crust over time. This result may occur because the wavelength of the imposed fault parallel loading is larger than the wavelengths of the other velocity components. The dominance of v_x depends on the level of preexisting damage. More damage produces larger and more temporally continuous regions of elevated v_y and v_z (Figure 9), suggesting that monitoring efforts may benefit from using all three components of motion in regions with relatively damaged host rock.

The shear strain fields tend to form larger and more temporally continuous regions of elevated strain than the volumetric fields throughout the full simulation time (Figure 12). However, in the simulation time immediately preceding fault reactivation, the areas and timespans of the strain components are similar to each other. The dominance of the continuity of the shear strain fields throughout the complete model time suggests that this strain component may provide more valuable precursory information than the volumetric strain throughout the interseismic period. However, in the days to months preceding fault reactivation, both strain components may provide similarly useful signals. Figure 13b shows the key components of this evolution.

Laboratory observations indicate that rocks dilate preceding macroscopic failure during triaxial compression (Brace, 1978; McBeck, Ben-Zion et al., 2021). Similarly, machine learning analyses suggest that dilation provides

more useful information about the proximity of macroscopic failure than shear strain in triaxial compression experiments (McBeck, Aiken et al., 2020). The strain components may provide slightly different predictive ability in these step over models and triaxial compression experiments because of the different loading conditions, and the difference in the desired prediction. The present models examine the velocity and strain fields preceding slip on the preexisting healed faults, and not the macroscopic failure of the system, when the macroscopic shear stress on the boundaries begins to decrease. In the laboratory experiments, in contrast, we used the local strain fields to predict the stress distance to macroscopic failure, when the rock core experiences a catastrophic stress drop (McBeck, Aiken et al., 2020). Moreover, the strain component that is most useful in predicting the timing of fault reactivation (the present work) and the timing of macroscopic failure in rocks without preexisting, system-scale faults (McBeck, Aiken et al., 2020) may differ. In rocks without preexisting weak zones, the fractures that propagate and coalesce to form faults may have rougher surfaces than systems with healed fault zones, such as these models. These rougher faults may then require more dilation in order for the surface to shear than smoother faults. The increasing dominance of volumetric strain toward fault reactivation in the simulations (Figure 12) further suggests the importance of fault opening preceding slip. In addition, the applied loading of the DEM models was dominated by the imposed right-lateral shear displacement. The imposed normal stresses produced smaller changes in the position of the boundaries than the shear displacement, implying that the influence of the shear displacement loading was stronger than the normal stress loading. Similarly, if the faults in the DEM models were not oriented parallel to the shear displacement loading, the predictive ability of the volumetric strain may be larger than the shear strain. If the faults were oriented at an oblique angle to the loading direction, a higher magnitude of dilation may be required for reactivation. Future work should examine the influence of the preexisting fault orientation relative to the loading direction on the relative magnitudes of the dilative and shear strain.

The evolving importance of the dilative strain in our simulations agrees with a global model of plate motions and strain rates along plate boundaries, neglecting transient changes (Kreemer et al., 2014). These interseismic plate velocities indicate that 28% of the plate boundaries host extensional deformation, while the remaining 72% host contraction. Near the San Andreas Fault System, the interseismic deformation is dominated by strike-slip motion, rather than contraction or extension (Wdowinski et al., 2001). In both the geodetic data and the numerical models presented here, the shear strain dominates deformation during the interseismic period leading to fault slip. However, recent evidence suggests that dilation accompanied slip during the Ridgecrest earthquake (e.g., Barnhart et al., 2020). Thus, shear strain may dominate deformation during the interseismic period, but both dilation and shear may occur during coseismic slip, consistent with our numerical models.

6. Conclusions

The numerical simulations suggest a similar likelihood of identification of precursors to fault slip both within and outside the fault zone, in contrast to the idea that precursors predominantly occur within the future fault zone. The fault configuration and amount of preexisting host rock damage control the ratio of on-fault and off-fault deformation, and thus the spatial distribution of precursors. Fault networks with larger steps and more distributed deformation produce relatively more off-fault deformation. This result agrees with observations of crustal fault networks (e.g., Milliner et al., 2015). The positive correlation between fault network complexity and off-fault damage observed in these numerical models and in crustal fault networks (e.g., Zinke et al., 2014) supports the idea that fault networks evolve in order to optimize the total mechanical efficiency of the system (e.g., Cooke & Madden, 2014).

Comparing the size of continuous regions of higher strains and velocity, in both time and space, facilitate the identification of the strain and velocity components that provide the most valuable precursory information. The results suggest that tracking the fault parallel velocity, v_x, may provide the most systematic information in fault networks dominated by fault-parallel shear loading. The fault parallel component generally produces larger and more temporally continuous regions of elevated deformation in the time before slip on the healed faults than the other components. Moreover, the difference between the area of this component and the other components increases toward failure, highlighting the value of tracking this component through time.

Examining the volumetric and shear strain fields indicates that the shear strain tends to host larger and more temporally continuous regions of elevated strain than the volumetric strain throughout the full simulation time, suggesting that the shear strain may be a more reliable indicator of approaching fault reactivation in these systems.

However, during the simulation time immediately preceding fault reactivation, the volumetric and shear strain fields produce similarly large and temporally continuous regions of elevated strain. Thus, in the days to months preceding fault reactivation, both the volumetric and shear strain may provide valuable precursory signals. This result agrees with observations of varying seismic wave properties preceding some large earthquakes (e.g., Malagnini et al., 2019), laboratory observations of the dilation of rocks under triaxial compression preceding macroscopic failure (Brace, 1978), machine learning analyses of the triaxial compression deformation of rock cores (McBeck, Aiken et al., 2020), statistical analyses of the partitioning of the strain components during triaxial compression (McBeck, Ben-Zion et al., 2020), and crustal observations of shear and dilative strain in interseismic (Kreemer et al., 2014) and seismic periods (Barnhart et al., 2020).

Data Availability Statement

The codes to build and run the models are available on Figshare (https://figshare.com/articles/software/DEM_models_of_shear_zones_with_rough_faults/18602327).

References

Abe, S., Place, D., & Mora, P. (2004). A parallel implementation of the lattice solid model for the simulation of rock mechanics and earthquake dynamics. *Pure and Applied Geophysics*, *161*(11), 2265–2277. https://doi.org/10.1007/s00024-004-2562-x

Abe, S., Van Gent, H., & Urai, J. L. (2011). DEM simulation of normal faults in cohesive materials. *Tectonophysics*, *512*(1–4), 12–21. https://doi.org/10.1016/j.tecto.2011.09.008

Allam, A. A., & Ben-Zion, Y. (2012). Seismic velocity structures in the southern California plate-boundary environment from double-difference tomography. *Geophysical Journal International*, *190*(2), 1181–1196. https://doi.org/10.1111/j.1365-246x.2012.05544.x

Andrews, D. J. (2005). Rupture dynamics with energy loss outside the slip zone. *Journal of Geophysical Research*, *110*(B1), B01307. https://doi.org/10.1029/2004jb003191

Bakun, W. H., Aagaard, B., Dost, B., Ellsworth, W. L., Hardebeck, J. L., Harris, R. A., et al. (2005). Implications for prediction and hazard assessment from the 2004 Parkfield earthquake. *Nature*, *437*(7061), 969–974. https://doi.org/10.1038/nature04067

Barnhart, W. D., Gold, R. D., & Hollingsworth, J. (2020). Localized fault-zone dilatancy and surface inelasticity of the 2019 Ridgecrest earthquakes. *Nature Geoscience*, *13*(10), 699–704. https://doi.org/10.1038/s41561-020-0628-8

Ben-Zion, Y. (2008). Collective behavior of earthquakes and faults: Continuum-discrete transitions, progressive evolutionary changes, and different dynamic regimes. *Reviews of Geophysics*, *46*(4), RG4006. https://doi.org/10.1029/2008rg000260

Ben-Zion, Y., Peng, Z., Okaya, D., Seeber, L., Armbruster, J. G., Ozer, N., et al. (2003). A shallow fault-zone structure illuminated by trapped waves in the Karadere–Duzce branch of the North Anatolian Fault, Western Turkey. *Geophysical Journal International*, *152*(3), 699–717. https://doi.org/10.1046/j.1365-246x.2003.01870.x

Ben-Zion, Y., & Sammis, C. G. (2003). Characterization of fault zones. *Pure and Applied Geophysics*, *160*(3), 677–715. https://doi.org/10.1007/pl00012554

Ben-Zion, Y., & Zaliapin, I. (2020). Localization and coalescence of seismicity before large earthquakes. *Geophysical Journal International*, *223*(1), 561–583. https://doi.org/10.1093/gji/ggaa315

Berg, S. S., & Skar, T. (2005). Controls on damage zone asymmetry of a normal fault zone: Outcrop analyses of a segment of the Moab fault, SE Utah. *Journal of Structural Geology*, *27*(10), 1803–1822. https://doi.org/10.1016/j.jsg.2005.04.012

Blank, D. G., & Morgan, J. K. (2019). Precursory stress changes and fault dilation lead to fault rupture: Insights from discrete element simulations. *Geophysical Research Letters*, *46*(6), 3180–3188. https://doi.org/10.1029/2018gl081007

Borcherdt, R. D., Johnston, M. J., Glassmoyer, G., & Dietel, C. (2006). Recordings of the 2004 Parkfield earthquake on the general earthquake observation system array: Implications for earthquake precursors, fault rupture, and coseismic strain changes. *Bulletin of the Seismological Society of America*, *96*(4B), S73–S89. https://doi.org/10.1785/0120050827

Brace, W. F. (1978). Volume changes during fracture and frictional sliding: A review. *Pure and Applied Geophysics*, *116*(4), 603–614. https://doi.org/10.1007/bf00876527

Chen, W. Y., Lovell, C. W., Haley, G. M., & sPyrak-Nolte, L. J. (1993). Variation of shear-wave amplitude during frictional sliding. *International Journal of Rock Mechanics and Mining Sciences & Geomechanics Abstracts*, *30*(7), 779–784. https://doi.org/10.1016/0148-9062(93)90022-6

Cheng, Y., Ross, Z. E., & Ben-Zion, Y. (2018). Diverse volumetric faulting patterns in the San Jacinto fault zone. *Journal of Geophysical Research: Solid Earth*, *123*(6), 5068–5081. https://doi.org/10.1029/2017jb015408

Cicerone, R. D., Ebel, J. E., & Britton, J. (2009). A systematic compilation of earthquake precursors. *Tectonophysics*, *476*(3–4), 371–396. https://doi.org/10.1016/j.tecto.2009.06.008

Cochran, E. S., Li, Y. G., Shearer, P. M., Barbot, S., Fialko, Y., & Vidale, J. E. (2009). Seismic and geodetic evidence for extensive, long-lived fault damage zones. *Geology*, *37*(4), 315–318. https://doi.org/10.1130/g25306a.1

Cooke, M. L., & Madden, E. H. (2014). Is the Earth lazy? A review of work minimization in fault evolution. *Journal of Structural Geology*, *66*, 334–346. https://doi.org/10.1016/j.jsg.2014.05.004

Cooke, M. L., Schottenfeld, M. T., & Buchanan, S. W. (2013). Evolution of fault efficiency at restraining bends within wet kaolin analog experiments. *Journal of Structural Geology*, *51*, 180–192. https://doi.org/10.1016/j.jsg.2013.01.010

Cunningham, W. D., & Mann, P. (2007). Tectonics of strike-slip restraining and releasing bends. *Geological Society, London, Special Publications*, *290*(1), 1–12. https://doi.org/10.1144/sp290.1

Del Castello, M., & Cooke, M. L. (2007). Underthrusting-accretion cycle: Work budget as revealed by the boundary element method. *Journal of Geophysical Research: Solid Earth*, *112*(B12). https://doi.org/10.1029/2007JB004997

DeLong, S. B., Hilley, G. E., Rymer, M. J., & Prentice, C. (2010). Fault zone structure from topography: Signatures of en echelon fault slip at mustang ridge on the San Andreas fault, Monterey County, California. *Tectonics*, *29*(5), TC5003. https://doi.org/10.1029/2010tc002673

Dieterich, J. H. (1978). Preseismic fault slip and earthquake prediction. *Journal of Geophysical Research*, *83*(B8), 3940–3948. https://doi.org/10.1029/jb083ib08p03940

Dolan, J. F., & Haravitch, B. D. (2014). How well do surface slip measurements track slip at depth in large strike-slip earthquakes? The importance of fault structural maturity in controlling on-fault slip versus off-fault surface deformation. *Earth and Planetary Science Letters*, *388*, 38–47. https://doi.org/10.1016/j.epsl.2013.11.043

Dooley, T. P., & Schreurs, G. (2012). Analogue modelling of intraplate strike-slip tectonics: A review and new experimental results. *Tectonophysics*, *574*, 1–71. https://doi.org/10.1016/j.tecto.2012.05.030

Dor, O., Rockwell, T. K., & Ben-Zion, Y. (2006). Geological observations of damage asymmetry in the structure of the san Jacinto, san Andreas and punchbowl faults in southern California: A possible indicator for preferred rupture propagation direction. *Pure and Applied Geophysics*, *163*(2), 301–349. https://doi.org/10.1007/s00024-005-0023-9

Faulkner, D. R., Mitchell, T. M., Healy, D., & Heap, M. J. (2006). Slip on 'weak' faults by the rotation of regional stress in the fracture damage zone. *Nature*, *444*(7121), 922–925. https://doi.org/10.1038/nature05353

Finzi, Y., & Langer, S. (2012). Damage in step-overs may enable large cascading earthquakes. *Geophysical Research Letters*, *39*(16), L16303. https://doi.org/10.1029/2012gl052436

Harris, R. A., & Day, S. M. (1993). Dynamics of fault interaction: Parallel strike-slip faults. *Journal of Geophysical Research*, *98*(B3), 4461–4472. https://doi.org/10.1029/92jb02272

Hedayat, A., Pyrak-Nolte, L. J., & Bobet, A. (2014). Precursors to the shear failure of rock discontinuities. *Geophysical Research Letters*, *41*(15), 5467–5475. https://doi.org/10.1002/2014GL060848

Herbert, J. W., Cooke, M. L., Oskin, M., & Difo, O. (2014). How much can off-fault deformation contribute to the slip rate discrepancy within the eastern California shear zone? *Geology*, *42*(1), 71–75. https://doi.org/10.1130/g34738.1

Jiao, L., Klinger, Y., & Scholtes, L. (2021). Fault segmentation pattern controlled by thickness of brittle crust. *Geophysical Research Letters*, *48*(19), e2021GL093390. https://doi.org/10.1029/2021gl093390

Kato, A., & Ben-Zion, Y. (2021). The generation of large earthquakes. *Nature Reviews Earth & Environment*, *2*(1), 26–39. https://doi.org/10.1038/s43017-020-00108-w

Kimurah, H., Itoh, Y., & Tsutsumi, H. (2004). Quaternary strike-slip crustal deformation around an active fault based on paleomagnetic analysis: A case study of the Enako fault in central Japan. *Earth and Planetary Science Letters*, *226*(3–4), 321–334. https://doi.org/10.1016/j.epsl.2004.08.003

Kreemer, C., Blewitt, G., & Klein, E. C. (2014). A geodetic plate motion and global strain rate model. *Geochemistry, Geophysics, Geosystems*, *15*(10), 3849–3889. https://doi.org/10.1002/2014gc005407

Lindsey, E. O., Fialko, Y., Bock, Y., Sandwell, D. T., & Bilham, R. (2014). Localized and distributed creep along the southern san Andreas Fault. *Journal of Geophysical Research: Solid Earth*, *119*(10), 7909–7922. https://doi.org/10.1002/2014JB011275

Lunn, R. J., Willson, J. P., Shipton, Z. K., & Moir, H. (2008). Simulating brittle fault growth from linkage of preexisting structures. *Journal of Geophysical Research*, *113*(B7), B07403. https://doi.org/10.1029/2007jb005388

Lyakhovsky, V., Ben-Zion, Y., & Agnon, A. (2001). Earthquake cycle, fault zones, and seismicity patterns in a rheologically layered lithosphere. *Journal of Geophysical Research*, *106*(B3), 4103–4120. https://doi.org/10.1029/2000jb900218

Malagnini, L., Dreger, D. S., Bürgmann, R., Munafò, I., & Sebastiani, G. (2019). Modulation of seismic attenuation at Parkfield, before and after the 2004 M6 earthquake. *Journal of Geophysical Research: Solid Earth*, *124*(6), 5836–5853. https://doi.org/10.1029/2019JB017372

Manighetti, I., Campillo, M., Bouley, S., & Cotton, F. (2007). Earthquake scaling, fault segmentation, and structural maturity. *Earth and Planetary Science Letters*, *253*(3–4), 429–438. https://doi.org/10.1016/j.epsl.2006.11.004

Manighetti, I., Mercier, A., & De Barros, L. (2021). Fault trace corrugation and segmentation as a measure of fault structural maturity. *Geophysical Research Letters*, *48*(20), e2021GL095372. https://doi.org/10.1029/2021gl095372

Mann, P. (2007). Global catalogue, classification and tectonic origins of restraining-and releasing bends on active and ancient strike-slip fault systems. *Geological Society, London, Special Publications*, *290*(1), 13–142. https://doi.org/10.1144/sp290.2

Mansfield, C., & Cartwright, J. (2001). Fault growth by linkage: Observations and implications from analogue models. *Journal of Structural Geology*, *23*(5), 745–763. https://doi.org/10.1016/s0191-8141(00)00134-6

McBeck, J., Aiken, J. M., Ben-Zion, Y., & Renard, F. (2020). Predicting the proximity to macroscopic failure using local strain populations from dynamic in situ X-ray tomography triaxial compression experiments on rocks. *Earth and Planetary Science Letters*, *543*, 116344. https://doi.org/10.1016/j.epsl.2020.116344

McBeck, J., Ben-Zion, Y., & Renard, F. (2020). The mixology of precursory strain partitioning approaching brittle failure in rocks. *Geophysical Journal International*, *221*(3), 1856–1872. https://doi.org/10.1093/gji/ggaa121

McBeck, J., Ben-Zion, Y., Zhou, X., & Renard, F. (2021). The influence of preexisting host rock damage on fault network localization. *Journal of Structural Geology*, *153*, 104471. https://doi.org/10.1016/j.jsg.2021.104471

McBeck, J., Cooke, M., Souloumiac, P., Maillot, B., & Mary, B. (2018). The influence of detachment strength on the evolving deformational energy budget of physical accretionary prisms. *Solid Earth*, *9*(6), 1421–1436. https://doi.org/10.5194/se-9-1421-2018

McClay, K., & Bonora, M. (2001). Analog models of restraining stepovers in strike-slip fault systems. *AAPG Bulletin*, *85*(2), 233–260.

Meng, H., & Fan, W. (2021). Immediate foreshocks indicating cascading rupture developments for 527 M 0.9 to 5.4 Ridgecrest earthquakes. *Geophysical Research Letters*, *48*(19), e2021GL095704. https://doi.org/10.1029/2021gl095704

Milliner, C. W., Dolan, J. F., Hollingsworth, J., Leprince, S., Ayoub, F., & Sammis, C. G. (2015). Quantifying near-field and off-fault deformation patterns of the 1992 Mw 7.3 Landers earthquake. *Geochemistry, Geophysics, Geosystems*, *16*(5), 1577–1598. https://doi.org/10.1002/2014gc005693

Milliner, C. W. D., Sammis, C., Allam, A. A., Dolan, J. F., Hollingsworth, J., Leprince, S., & Ayoub, F. (2016). Resolving fine-scale heterogeneity of co-seismic slip and the relation to fault structure. *Scientific Reports*, *6*(1), 1–9. https://doi.org/10.1038/srep27201

Nelson, M. R., & Jones, C. H. (1987). Paleomagnetism and crustal rotations along a shear zone, Las Vegas Range, southern Nevada. *Tectonics*, *6*(1), 13–33. https://doi.org/10.1029/TC006i001p00013

Niu, F., Silver, P. G., Daley, T. M., Cheng, X., & Majer, E. L. (2008). Preseismic velocity changes observed from active source monitoring at the Parkfield SAFOD drill site. *Nature*, *454*(7201), 204–208. https://doi.org/10.1038/nature07111

Nur, A. (1972). Dilatancy, pore fluids, and premonitory variations of t_s/t_p travel times. *Seismological Society of America Bulletin*, *62*(5), 1217–1222. https://doi.org/10.1785/bssa0620051217

Ohnaka, M. (1996). Nonuniformity of the constitutive law parameters for shear rupture and quasistatic nucleation to dynamic rupture: A physical model of earthquake generation processes. *Proceedings of the National Academy of Sciences*, *93*(9), 3795–3802. https://doi.org/10.1073/pnas.93.9.3795

Okubo, K., Rougier, E., Lei, Z., & Bhat, H. S. (2020). Modeling earthquakes with off-fault damage using the combined finite-discrete element method. *Computational Particle Mechanics*, *7*(5), 1057–1072. https://doi.org/10.1007/s40571-020-00335-4

Oskin, M., Perg, L., Blumentritt, D., Mukhopadhyay, S., & Iriondo, A. (2007). Slip rate of the calico fault: Implications for geologic versus geodetic rate discrepancy in the Eastern California shear zone. *Journal of Geophysical Research*, *112*(B3), B03402. https://doi.org/10.1029/2006JB004451

Otsuki, K., & Dilov, T. (2005). Evolution of hierarchical self-similar geometry of experimental fault zones: Implications for seismic nucleation and earthquake size. *Journal of Geophysical Research*, *110*(B3), B03303. https://doi.org/10.1029/2004JB003359

Peacock, D. C. P., & Sanderson, D. J. (1991). Displacements, segment linkage and relay ramps in normal fault zones. *Journal of Structural Geology*, *13*(6), 721–733. https://doi.org/10.1016/0191-8141(91)90033-f

Place, D., Lombard, F., Mora, P., & Abe, S. (2002). Simulation of the microphysics of rocks using LSM Earth. *Pure and Applied Geophysics*, *159*(9), 1911–1932. https://doi.org/10.1007/s00024-002-8715-x

Rice, J. R., Sammis, C. G., & Parsons, R. (2005). Off-fault secondary failure induced by a dynamic slip pulse. *Bulletin of the Seismological Society of America*, *95*(1), 109–134. https://doi.org/10.1785/0120030166

Riedel, W. (1929). Zur Mechanik geologischer Brucherscheinungen ein Beitrag zum Problem der Fiederspaten. In *Zentralblatt Fur Mineralogie, Geologie und Paleontologie* (pp. 354–368).

Rockwell, T. K., Lindvall, S., Dawson, T., Langridge, R., Lettis, W., & Klinger, Y. (2002). Lateral offsets on surveyed cultural features resulting from the 1999 Izmit and Duzce earthquakes, Turkey. *Bulletin of the Seismological Society of America*, *92*(1), 79–94. https://doi.org/10.1785/0120000809

Scott, C. P., Arrowsmith, J. R., Nissen, E., Lajoie, L., Maruyama, T., & Chiba, T. (2018). The M7 2016 Kumamoto, Japan, earthquake: 3-D deformation along The fault and within the damage zone constrained from differential lidar topography. *Journal of Geophysical Research: Solid Earth*, *123*(7), 6138–6155. https://doi.org/10.1029/2018jb015581

Shelef, E., & Oskin, M. (2010). Deformation processes adjacent to active faults: Examples from eastern California. *Journal of Geophysical Research*, *115*(B5), B05308. https://doi.org/10.1029/2009JB006289

Shreedharan, S., Bolton, D. C., Rivière, J., & Marone, C. (2020). Preseismic fault creep and elastic wave amplitude precursors scale with lab earthquake magnitude for the continuum of tectonic failure modes. *Geophysical Research Letters*, *47*(8), e2020GL086986. https://doi.org/10.1029/2020gl086986

Spudich, P., & Olsen, K. B. (2001). Fault zone amplified waves as a possible seismic hazard along the Calaveras fault in central California. *Geophysical Research Letters*, *28*(13), 2533–2536. https://doi.org/10.1029/2000gl011902

Teran, O. J., Fletcher, J. M., Oskin, M. E., Rockwell, T. K., Hudnut, K. W., Spelz, R. M., et al. (2015). Geologic and structural controls on rupture zone fabric: A field-based study of the 2010 Mw 7.2 El Mayor–Cucapah earthquake surface rupture. *Geosphere*, *11*(3), 899–920. https://doi.org/10.1130/ges01078.1

Titus, S. J., Dyson, M., DeMets, C., Tikoff, B., Rolandone, F., & Bürgmann, R. (2011). Geologic versus geodetic deformation adjacent to the San Andreas fault, central California. *GSA Bulletin*, *123*(5–6), 794–820. https://doi.org/10.1130/b30150.1

Trudgill, B., & Cartwright, J. (1994). Relay-ramp forms and normal-fault linkages, Canyonlands National Park, Utah. *The Geological Society of America Bulletin*, *106*(9), 1143–1157. https://doi.org/10.1130/0016-7606(1994)106<1143:rrfanf>2.3.co;2

Wdowinski, S., Sudman, Y., & Bock, Y. (2001). Geodetic detection of active faults in S. California. *Geophysical Research Letters*, *28*(12), 2321–2324. https://doi.org/10.1029/2000gl012637

Wechsler, N., Rockwell, T. K., & Ben-Zion, Y. (2009). Application of high resolution DEM data to detect rock damage from geomorphic signals along the central San Jacinto Fault. *Geomorphology*, *113*(1–2), 82–96. https://doi.org/10.1016/j.geomorph.2009.06.007

Wesnousky, S. G. (2006). Predicting the endpoints of earthquake ruptures. *Nature*, *444*(7117), 358–360. https://doi.org/10.1038/nature05275

Whitcomb, J. H., Garmany, J. D., & Anderson, D. L. (1973). Earthquake prediction: Variation of seismic velocities before the San Francisco earthquake. *Science*, *180*(4086), 632–635. https://doi.org/10.1126/science.180.4086.632

Wollin, C., Bohnhoff, M., Martínez-Garzón, P., Küperkoch, L., & Raub, C. (2018). A unified earthquake catalogue for the Sea of Marmara Region, Turkey, based on automatized phase picking and travel-time inversion: Seismotectonic implications. *Tectonophysics*, *747*, 416–444. https://doi.org/10.1016/j.tecto.2018.05.020

Xu, S., Ben-Zion, Y., Ampuero, J. P., & Lyakhovsky, V. (2015). Dynamic ruptures on a frictional interface with off-fault brittle damage: Feedback mechanisms and effects on slip and near-fault motion. *Pure and Applied Geophysics*, *172*(5), 1243–1267. https://doi.org/10.1007/s00024-014-0923-7

Zigone, D., Ben-Zion, Y., Campillo, M., & Roux, P. (2015). Seismic tomography of the Southern California plate boundary region from noise-based Rayleigh and Love waves. *Pure and Applied Geophysics*, *172*(5), 1007–1032. https://doi.org/10.1007/s00024-014-0872-1

Zinke, R., Hollingsworth, J., & Dolan, J. F. (2014). Surface slip and off-fault deformation patterns in the 2013 MW 7.7 Balochistan, Pakistan earthquake: Implications for controls on the distribution of near-surface coseismic slip. *Geochemistry, Geophysics, Geosystems*, *15*(12), 5034–5050. https://doi.org/10.1002/2014gc005538